Parallel Prefrontal Pathways Reach Distinct Excitatory and Inhibitory Systems in Memory-Related Rhinal Cortices

Jamie G. Bunce,[1] Basilis Zikopoulos,[1] Marcia Feinberg,[1] and Helen Barbas[1,2]*

[1]Neural Systems Lab, Department of Health Sciences, Boston University, Boston, Massachusetts 02215
[2]Graduate Program in Neuroscience, Boston University, and Boston University School of Medicine, Boston, Massachusetts 02215

ABSTRACT

To investigate how prefrontal cortices impinge on medial temporal cortices we labeled pathways from the anterior cingulate cortex (ACC) and posterior orbitofrontal cortex (pOFC) in rhesus monkeys to compare their relationship with excitatory and inhibitory systems in rhinal cortices. The ACC pathway terminated mostly in areas 28 and 35 with a high proportion of large terminals, whereas the pOFC pathway terminated mostly through small terminals in area 36 and sparsely in areas 28 and 35. Both pathways terminated in all layers. Simultaneous labeling of pathways and distinct neurochemical classes of inhibitory neurons, followed by analyses of appositions of presynaptic and postsynaptic fluorescent signal, or synapses, showed overall predominant association with spines of putative excitatory neurons, but also significant interactions with presumed inhibitory neurons labeled for calretinin, calbindin, or parvalbumin. In the upper layers of areas 28 and 35 the ACC pathway was associated with dendrites of neurons labeled with calretinin, which are thought to disinhibit neighboring excitatory neurons, suggesting facilitated hippocampal access. In contrast, in area 36 pOFC axons were associated with dendrites of calbindin neurons, which are poised to reduce noise and enhance signal. In the deep layers, both pathways innervated mostly dendrites of parvalbumin neurons, which strongly inhibit neighboring excitatory neurons, suggesting gating of hippocampal output to other cortices. These findings suggest that the ACC, associated with attention and context, and the pOFC, associated with emotional valuation, have distinct contributions to memory in rhinal cortices, in processes that are disrupted in psychiatric diseases. J. Comp. Neurol. 521:4260–4283, 2013.

© 2013 Wiley Periodicals, Inc.

Classical studies have shown that information from multiple sensory association cortices converges on medial temporal lobe cortices in the rhinal region which include areas 28, 35, and 36 (Van Hoesen et al., 1972; Van Hoesen and Pandya, 1975; Steward and Scoville, 1976), a critical hub for long-term episodic memory (Squire and Zola-Morgan, 1991; Mishkin and Murray, 1994; Squire and Zola, 1996; Suzuki, 2006). Pathways from sensory association cortices reach first the most lateral area of the rhinal region (area 36), and from there information cascades through sequential steps to rhinal area 35 and then to the superficial layers of area 28 (entorhinal cortex), the most medial rhinal area and the major relay to the hippocampus (Van Hoesen et al., 1972; Steward and Scoville, 1976; Wellman and Rockland, 1997; Burwell and Amaral, 1998; Blatt et al.,

2003; Lavenex et al., 2004; Mohedano-Moriano et al., 2007, 2008; Insausti and Amaral, 2008). Projection neurons from the upper layers (II–III) of entorhinal area 28 convey cortical input to the hippocampus (Anderson

and Lomo, 1966; Witter et al., 1989; Wirth et al., 2003; Suzuki, 2007).

The output of the hippocampus, in turn, innervates neurons in the deep layers (V–VI) of entorhinal cortex, which project back to the cortex, in pathways thought to have a role in memory storage (Kosel et al., 1982; Swanson and Kohler, 1986; Burwell and Amaral, 1998; Lavenex et al., 2002; Munoz and Insausti, 2005). Specific rhinal cortices may underlie unique elements of mnemonic function (Davachi et al., 2003; Buffalo et al., 2006; Bachevalier and Nemanic, 2008), serving the relational processes necessary for episodic memory (Lavenex and Amaral, 2000; Manns and Eichenbaum, 2006; Murray and Wise, 2012).

Prefrontal cortices on the medial wall of the hemisphere in the anterior cingulate cortex (ACC), as well as the posterior orbitofrontal cortex (pOFC) on the basal surface have bidirectional connections with rhinal cortices (Pandya et al., 1981; Barbas, 1993; Carmichael and Price, 1995; Rempel-Clower and Barbas, 2000; Kondo et al., 2005; Saleem et al., 2008). Both of these prefrontal regions receive robust projections from the hippocampal formation (e.g., Rosene and Van Hoesen, 1977; Barbas and Blatt, 1995; Cavada et al., 2000; Munoz and Insausti, 2005), but do not project directly to the hippocampus, suggesting that reciprocal communication with the hippocampus occurs through rhinal cortices, in general, and area 28, in particular (but see Rockland and Van Hoesen, 1999).

The pOFC (areas OPro and 13), a multimodal region, is thought to have a role in emotional valuation of stimuli (reviewed in Barbas, 2000a, 2000b, 2007) while the

ACC (area 32 and anterior area 24) has a role in monitoring ongoing behavior pertaining to memory of previously learned outcomes (MacDonald et al., 2000; Botvinick et al., 2004; Rushworth et al., 2007; reviewed in Weible, 2013). Specifically, the ACC is thought to monitor the context of signals, keep track of the consequences of recently made choices, signal attentional incongruence or unexpected outcomes, and allocate attentional resources accordingly (Hayden and Platt, 2006; Kennerley et al., 2006; Sallet et al., 2007; Rudebeck et al., 2008; Kaping et al., 2011; Ferdinand et al., 2012; Hyman et al., 2012).

Pathways from pOFC and ACC reach in a complementary fashion the rhinal region, the ACC has an additional projection to parahippocampal areas TH and TF (Van Hoesen et al., 1975; Carmichael and Price, 1995; Rempel-Clower and Barbas, 2000; Kondo et al., 2003, 2005; Saleem et al., 2008; Bunce and Barbas, 2011), but how each of these functionally distinct prefrontal regions impinges on areas associated with memory is not well understood. An overarching hypothesis is that the concerted projection from prefrontal cortices may underlie the integration of information about emotional significance and context (Clark et al., 2012) to mediate what fraction of information is remembered.

Here we addressed several unanswered questions beyond the known topography of terminations of prefrontal pathways. To what extent do the functionally distinct pOFC and ACC target the input (upper) and output (deep) layers of memory-related rhinal cortices? Are there differences in the size of terminals in rhinal cortices, correlated with synaptic efficacy, from the two prefrontal regions? Importantly, do terminals from each of the two prefrontal pathways target in similar proportions, or not, functionally distinct classes of inhibitory neurons in rhinal cortices?

These questions are based on evidence that signal transfer to and from the hippocampus through the rhinal cortices is not a passive process. Sensory information arriving in the superficial layers of the rhinal cortices must overcome robust local inhibition to gain access to the hippocampus (Biella et al., 2002; de Curtis and Paré, 2004). Thus, information arriving in entorhinal area 28 is propagated to the hippocampus with low probability (Pelletier et al., 2004), suggesting that the memory circuit is effectively gated from information overload. Interaction of pathways with inhibitory as well as excitatory neurons in rhinal cortices is thus critical for a filtering process. Here we investigated the pathway interactions from ACC and pOFC cortices with excitatory and inhibitory neurons in the rhinal cortices from the level of the system to the synapse. Our findings suggest that prefrontal areas that specialize in signaling

Abbreviations

|	
ACC	Anterior cingulate cortex
AB	Avidin-biotin
At	Axon terminal
BDA	Biotinylated dextran amine
BSA	Bovine serum albumin
BSA-C	acetylated BSA
CB	Calbindin
CBl	Cascade blue
CCD	Charge-coupled device
CR	Calretinin
DAB	Diaminobenzidine
EM	Electron microscope
FE	Fluoroemerald
HRP	Horseradish peroxidase
LY	Lucifer yellow
NGS	Normal goat serum
NHS	Normal horse serum
PaS:	Parasubiculum
pOFC	Posterior orbitofrontal cortex
PrS:	Presubiculum
PV	Parvalbumin
PB	Phosphate buffer
PBS	Phosphate buffered saline
PSD	Postsynaptic density
Sd	Standard deviation
Sp	Spine
TMB	Tetramethylbenzidine
WM	White matter
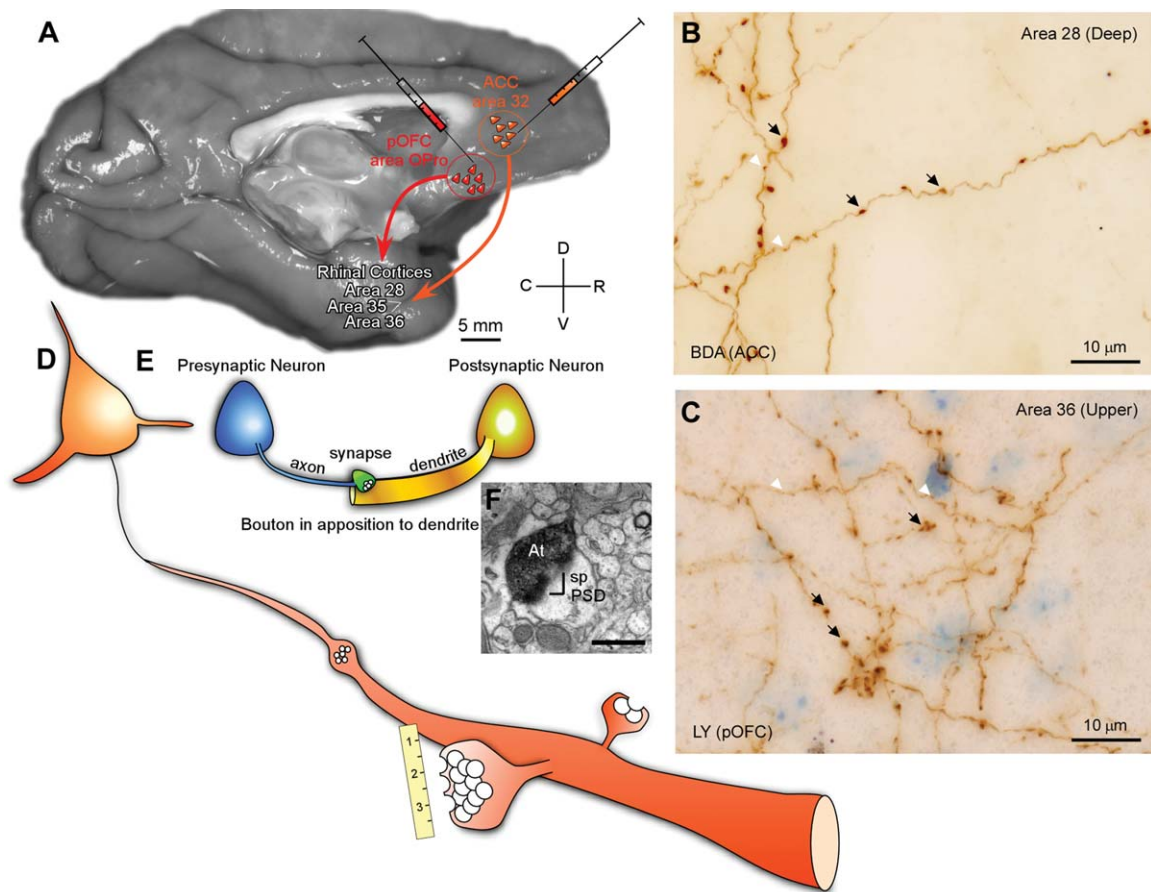
Figure 1. Overview of experimental design. **A:** Anterograde tracers were injected in ACC area 32 of the medial prefrontal cortex or OPro/posterior area 13 of the pOFC in rhesus monkeys (*Macaca mulatta*). **B–D:** Large and small labeled boutons were mapped and quantified in rhinal areas 28, 35, and 36 of the medial temporal lobe using a combination of exhaustive sampling and stereological techniques (in B,C, large boutons are denoted by black arrows and small boutons by white arrowheads). Adjacent sections of tissue through the rhinal cortices were processed to view tracer as well as the calcium binding proteins PV, CB, or CR using triple labeling immunohistochemistry for fluorescence. Analysis at the fluorescence microscope identified boutons in apposition to postsynaptic targets schematically represented in **E**. Putative inhibitory postsynaptic targets were identified by morphological characteristics or neurochemical staining against CB and PV at the electron microscope **(F)**. At, axon terminal; BDA, biotinylated dextran amine; LY, Lucifer yellow; PSD, postsynaptic density; sp, spine. Scale bar = 0.5 μm in F.

the value and context of information to be remembered may have facilitated access to the hippocampus.

MATERIALS AND METHODS

Figure 1A–F shows the essence of our experimental approach.

Animals

Studies were conducted on eight young adult (2.0–3.0 years of age) rhesus monkeys (*Macaca mulatta*) of both sexes weighing 3.2–4.5 kg. Analyses were based on nine tracer injections (three biotinylated dextran amine, four lucifer yellow, one fluoroemerald, one cascade blue; see Table 1). Experiments were conducted in accordance with the National Institutes of Health (NIH) *Guide for the Care and Use of Laboratory Animals*,

and every effort was made to minimize pain or distress and the number of animals used for each study. A detailed protocol was approved by the Institutional Animal Care and Use Committee (IACUC) at Boston University, Harvard Medical School (for New England Primate

TABLE 1.

Anterograde Tracer Injections in the Prefrontal Cortex

Case	Area Injected	Tracer
BG	Area 32	BDA
BI-R	Area 32	BDA
BI-R	Area 32	FE
AY	Area 32	BDA
BL	Area 32	LY
BN	Area 32	LY
BI-L	Area 13	LY
BK	OPro	CBl
BJ	OPro	LY

TABLE 2.
Antibodies Used in the Present Study

Antigen	Immunogen	Source	Product #	Dillution
Lucifer Yellow	Keyhole limpet hemocyanin	Molecular Probes; rabbit polyclonal IgG	A5750	1:800
Fluoroscein	Keyhole limpet hemocyanin	Molecular Probes; rabbit polyclonal IgG	A889	1:800
Cascade Blue	Keyhole limpet hemocyanin	Molecular Probes; rabbit polyclonal IgG	A5760	1:800
Parvalbumin	Rat muscle parvalbumin	Swant Antibodies, rabbit polyclonal, lot#5.10	PV 25	1:2000
	Purified carp muscle parvalbmin	Swant Antibodies, mouse monoclonal, lot#10-11(F)	235	1:2000
	Rat muscle parvalbumin	Swant Antibodies goat, lot#3.6	PVG-214	1:5000
Calbindin D-28	Purified chicken calbindin D-28k	Swant Antibodies, mouse monoclonal, lot#07(F)	300	1:2000
	Rat recombinant calbindin D-28k	Swant Antibodies, rabbit, lot#9.03	CB 38	1:2000
Calretinin	Human recombinant calretinin	Swant Antibodies, goat, lot#1§.1	CG1	1:2000
	Human recombinant calretinin	Swant Mouse mouse monoclonal, lot#010399	6B3	1:2000

Research Center [NEPRC]), and Massachusetts General Hospital (for Imaging), as being consistent with humane treatment of animals. Animals were housed at NEPRC before and after surgery, and up to euthanasia.

Brain imaging

About 1 week prior to surgery, we conducted magnetic resonance imaging (MRI) to guide the injection of neural tracers during surgery. For imaging, the monkey was sedated with propofol (loading dose, 2.5–5 mg/kg intravenous; continuous rate infusion, 0.25–0.4 mg/kg^{-1} min^{-1}) and positioned in a nonmetallic stereotaxic device. MRI was performed with a 3 T superconducting magnet (Phillips; or Siemens). A T1-weighted 3D SPGR (TR70, TE6, flip 45) was obtained through the brain, using a 512 × 384 matrix and a 16 × 16 field of view (FOV). Section thickness ranged from 0.65 to 1 mm with no gaps between successive sections.

Surgical procedure to inject neural tracers

About 1 week after imaging we performed surgery to inject neural tracers under general anesthesia. The monkeys were sedated with ketamine hydrochloride (10–15 mg/kg, intramuscularly), then deeply anesthetized with gas anesthetic (isoflurane), until a surgical level of anesthesia was achieved. Heart rate, muscle tone, and respiration were evaluated to maintain a surgical level of anesthesia. Surgery was performed under sterile conditions with the monkey's head held by a stereotaxic apparatus. A craniotomy was made on the dorsal surface of the skull over the site for injection, the dura retracted, and the cortex exposed. Tracer injections were made using a microsyringe (5 or 10 μl, Hamilton, Reno, NV) mounted on a microdrive following coordinates calculated from the MRI. The bidirectional tracers biotinylated dextran amine (BDA), lucifer yellow (LY), fluoroemerald (FE), and cascade blue (CBl) were of 10 kDa molecular weight, optimized for anterograde labeling (Veenman et al., 1992; Miller and Schreiner, 2000). For each injection site, the dye was diluted to 10 mg/ml in distilled water and delivered in 2–4 penetrations spaced 0.5 mm apart, to inject a total volume of up to 5 μl. For injections in area 32 the injection needle passed through dorsomedial area 9. For the injections in pOFC the needle passed through dorsal and lateral cortices and the underlying white matter. Spread of tracer to other areas in the path of the needle was avoided or minimized by thoroughly rinsing the needle and bevel before insertion in the brain, and retracting the needle at least 5–10 minutes after completion of each injection to allow absorption of the dye locally. After injection of neural tracers, the wound was closed and the animal was given antibiotics and analgesics (buprenex, 0.01 mg/kg).

Perfusion and tissue processing

After a survival period of 19 days, which allowed the dyes to travel from the injection site to axon terminals, the animal was given an overdose of anesthetic (sodium pentobarbitol, >50 mg/kg, to effect) and perfused with 4% paraformaldehyde, 0.2% glutaraldehyde in 0.1 M phosphate buffer (PB; pH 7.4) at 37°C. The brain was removed and cryoprotected in increasing concentrations of sucrose (10%, 15%, 20%, 25%, in 0.01 M phosphate-buffered saline [PBS]). The brain was then frozen by immersion in isopentane for rapid and uniform freezing at −70°C and cut in the coronal plane at 50-μm sections in 10 matched series on a freezing microtome. To preserve the ultrastructure, tissue was stored at −20°C in antifreeze solution (30% ethylene glycol, 30% glycerol, 40% 0.05M PB, pH 7.4 with 0.05% sodium azide).

Antibody characterization

The primary antibodies used in this study are listed in Table 2. Antibodies against the neural tracers LY, FE, and CBl have been used previously and are well characterized to label neurons, axons, and terminal boutons with LY (Stewart, 1981; Saleem et al., 2008), FE (Medalla and Barbas, 2012; Zikopoulos and Barbas, 2012) and CBl (May and Hill, 2006; Mangold and Hill, 2008).

The distribution of converted tracer was consistent with that observed in unprocessed adjacent sections assessed at the fluorescence microscope.

The parvalbumin rabbit polyclonal antibody (PV 25, Swant, Switzerland) specificity has been demonstrated with various methods (Celio and Heizmann, 1981) and crossreacts with many species including human parvalbumin (data sheet from manufacturer). The distribution of label we observed was consistent with that previously described in the monkey cortex (Saleem and Logothetis, 2007).

The parvalbumin mouse antibody (235, Swant) reacts with tissue from monkey and specifically stains the ^{45}Ca-binding spot of parvalbumin (MW 12,000 and IEF 4.9) in a 2D immunoblot (Celio et al., 1988; product sheet from the manufacturer). This antibody has previously been used to label GABAergic neurons in primates (Imura and Rockland, 2006). The distribution of labeled cortical neurons matched previous descriptions in macaque monkeys (Saleem and Logothetis, 2007).

The parvalbumin goat antibody (PVG-214, Swant) reacts with tissue from monkeys (Macaca fascicularis) and stains a band at $\sim$12 kDa (Schwaller et al., 1999; product sheet from manufacturer). This antibody has been previously used to label inhibitory neurons in the rat cortex and amygdala (Rostkowski et al., 2009; Xu et al., 2010).

The calbindin D-28k mouse antibody (300, Swant) reacts with tissue from monkeys (Macaca fascicularis) and stains a band at $\sim$28 kDa (Celio et al., 1990; product sheet from manufacturer). This antibody has been previously used to label inhibitory neurons in the monkey brain (Saunders et al., 2012). The distribution of labeled cells we observed matched previous descriptions in the monkey temporal lobe (Lavenex et al., 2009).

The calbindin D-28k rabbit antibody (CB38, Swant) reacts with tissue from monkeys (Macaca fascicularis) and stains a band at $\sim$28 kDa (Airaksinen et al., 1997; product sheet from manufacturer). The antibody has been used to label neurons in the monkey retina (Majumdar et al., 2008; Hirano et al., 2011). The distribution of labeled CB neurons matched previous descriptions in the monkey temporal lobe (Lavenex et al., 2009).

The calretinin goat antibody (CG1, Swant) stains a band at $\sim$29 kDa (Schiffmann et al., 1999). We observed a similar distribution of labeled cortical inhibitory neurons as previously described in the monkey cortex (Disney and Aoki, 2008).

The calretinin mouse monoclonal antibody (6B3, Swant) reacts with tissue from monkeys (Macaca fascicularis) and stains a band at $\sim$29 kDa (Zimmermann

and Schwaller, 2002; product sheet from manufacturer). We observed a similar pattern of neuronal labeling as has been reported in the monkey medial temporal cortices (Lavenex et al., 2009).

Immunohistochemistry to visualize boutons labeled with BDA/LY/FE/CBI

We used the avidin–biotin (AB) with horseradish peroxidase (HRP) method (Vectastain PK-6100 ABC Elite kit, Vector Laboratories, Burlingame, CA). All assays were conducted at 4°C. Free-floating brain sections were washed in 0.01 M PBS and then incubated in 0.05 M glycine and preblocked in 5% normal goat serum (NGS) and 5% bovine serum albumin (BSA) with 0.2% Triton X. Sections with BDA were incubated in AB-HRP solution for 1 hour (1:100 in PBS containing 0.1% Triton-X). The tissue was rinsed and processed using the peroxidase-catalyzed polymerization of diaminobenzidine (DAB; 0.05% DAB, and 0.004% H_2O_2 in PBS) for 2–3 minutes (DAB kit, Vector or Zymed Laboratories, South San Francisco, CA). Sections with fluorescent tracer were incubated overnight in antibody against LY, FE, or CBI (1:800, in PBS, 1% NGS, 1% BSA, 0.1% Triton-X; rabbit polyclonal, Molecular Probes, Eugene, OR), followed by incubation in secondary biotinylated goat antirabbit IgG (1:200, for 2 hours; Vector Laboratories), then in AB-HRP and DAB as previously described. Following processing, sections were rinsed, mounted on gelatin-coated slides, dried, dehydrated in graded alcohols, cleared in xylenes, and coverslipped with Permount or Entelan. Every other section was counterstained with thionin (Sigma, St. Louis, MO) to define areal and laminar boundaries. We used the same procedure to process BDA, LY, and CBI tissue for electron microscopy (EM), but with 0.025% Triton-X to preserve the ultrastructure.

Triple immunohistochemical fluorescence labeling for confocal microscopy

Triple fluorescence labeling for confocal microscopy was used to investigate pathway interactions of multiple pre- and postsynaptic targets. We used triple labeling immunohistochemical methods to label tracer and PV/CB/CR-positive postsynaptic elements with fluorescent secondary antibodies. Sections were coincubated with antibodies against LY, FE, or CBI (1:800, in PBS, 0.1% BSA-C, 1% NHS, 0.1% Triton-X; rabbit polyclonal, Molecular Probes, Grand Island, NY), and CB (1:2,000, developed in mouse, Swant), PV (1:5,000, developed in goat, Swant), or CR (1:2,000, developed in goat; 1:2,000 developed in mouse; Swant) followed by incubation in fluorescent secondary antibodies Alexa 350; Alexa 488,

Alexa 568, or Alexa 647 (1:100 or 1:200, in PBS, 0.1% BSA-C, 1% NHS, 0.1% Triton-X, developed in donkey, Molecular Probes). Sections were mounted wet and coverslipped with ProLong Gold Antifade (Invitrogen, Grand Island, NY).

Triple preembedding immunohistochemical labeling for EM

We used triple labeling preembedding immunohistochemistry for serial electron microscopy to investigate pathway interactions of multiple pre- and postsynaptic elements. Preembedding labeling has the advantage of strong, specific labeling due to easier penetration of reagents in free-floating sections, before they are dehydrated and embedded in resin. We used triple immunohistochemical methods to label neural tracers with DAB (above) and parvalbumin (PV) or calbindin (CB) neurons with either silver-enhanced gold-conjugated or tetramethylbenzidine (TMB)-labeled secondary antibodies. These methods show distinct labeling at the EM: DAB appears as a dark uniform precipitate, silver-enhanced gold particles as circular clumps of variable size, and TMB as rod-shaped crystals (e.g., Gonchar and Burkhalter, 2003; Pinto et al., 2003; Moore et al., 2004; Zikopoulos and Barbas, 2007).

After labeling fibers with DAB, sections were incubated in AB blocking reagent to prevent crossreaction with other biotinylated secondary antibodies visualized with TMB. For BDA, LY, or CBl-labeled tissue, sections were coincubated overnight in the primary antibodies for PV (1:2,000, rabbit polyclonal) and CB (1:2,000 mouse polyclonal; Swant) and then in biotinylated anti-mouse IgG (1:200, for 2 hours; Vector Laboratories) followed by AB-HRP. Sections were postfixed in 6% glutaraldehyde with 2% paraformaldehyde using a variable wattage microwave (3–6 minutes at 150W in the Biowave; Ted Pella, Redding, CA) until the fixative temperature reached 30°C. Gold labeling was intensified with silver (6–12 minutes; IntenSE M kit, Amersham, Pittsburgh, PA), which results in aggregates of gold particles of variable sizes. Sections were processed for TMB, then stabilized with DAB-cobalt chloride solution. In control experiments we omitted primary antibodies to test the specificity of secondary antibodies and used the AB blocking kit prior to AB binding to test the specificity of labeling.

After labeling we cut small pieces of cortex (all layers) with anterograde label in areas 28, 35, and 36. These pieces were postfixed in reduced osmium, followed by a straight osmium solution, rinsed, dehydrated in increasing concentrations of ethanol (50–100%), which included *en bloc* staining with 1% uranyl acetate

(EM Sciences, Hatfield, PA) infiltrated with propylene oxide during the 70% stage, and flat embedded in LX112 (Ladd Research Industries, Williston, VT) or Araldite (Earnest F. Fullam, Redding, CA) using aclar plastic (Ted Pella). Pieces of aclar-embedded tissue were cut and reembedded in resin blocks and sectioned at 50 nm with a diamond knife (Diatome USA, Hatfield, PA) using an ultramicrotome (Ultracut, Leica, Wein, Austria). Serial ultrathin sections were collected on single slot pioloform-coated grids.

Data analysis
Population analysis
Photomicrographs of labeled boutons in the rhinal cortices were captured at the light microscope using a high-resolution CCD camera (Olympus DP70). We acquired image stacks of multiple focal planes to create pictures through the entire thickness of the sections in the z-axis using ImageJ (v. 132j for Windows; NIH) as described (Medalla and Barbas, 2006; Zikopoulos and Barbas, 2006). To obtain population estimates of bouton size we captured images at high magnification (1,000×) of >3 random sites within a region of anterograde label in the upper and deep layers of areas 28, 35, and 36. Within each stack of images, we manually traced the profile of each labeled bouton to measure the major diameter using ImageJ.

Quantitative mapping: light microscope analysis
We collected all data quantitatively using exhaustive sampling or unbiased stereologic procedures and conducted analyses using conventional statistics. We mapped labeled boutons in rhinal cortices in precise register with respect to anatomic landmarks using a workstation with an encoded microscope stage interfaced to a computer using commercial software (Neurolucida, MicroBrightField, Williston, VT). Exhaustive sampling of labeled boutons was achieved by using a meander scan feature to systematically progress through the entirety of each area. The exhaustive sampling data included bouton frequencies and calculations for area, which were used to calculate the relative density of boutons per unit area (mm^2). We estimated bouton density in all areas using exhaustive sampling or stereologic procedures aided by a semiautomated system (StereoInvestigator, MicroBrightField), as described (e.g., Germuska et al., 2006; Medalla et al., 2007; Zikopoulos and Barbas, 2007). For each area, at least three evenly spaced sections were selected using systematic random sampling to count boutons in different laminar compartments (superficial layers I–III and deep layers IV–VI). The stereological data included volume calculation for each laminar group with the Cavalieri method,

which takes into consideration the area of the layer and thickness of each section. We counted boutons using an optical disector restricted to the central fraction of the tissue thickness (11 μm). The top and bottom of each section (minimum 2 μm for 15-μm sections after shrinkage) thus were used as guard zones to avoid error due to possible uneven tissue sectioning. The actual thickness of mounted sections was measured by the program at each counting site. The counting frame/disector size (area 40 × 40 μm; height = 11 μm) and grid spacing (ranging from 100 × 100 μm to 400 × 400 μm) were set to employ a sampling fraction to yield a coefficient of error of ≤10%, as recommended (Gundersen et al., 1988; Howard and Reed, 1998). The stereological analysis yielded estimates of the total number of boutons in each laminar group and the volume of the laminar group examined. The volume estimates along with the total estimates of boutons were used to calculate the density of boutons per unit volume (mm^3). To account for variability of labeling due to differences in the size of the injections and to compare the relative laminar distribution of terminations among cases analyzed for each injection site we normalized data as follows: the relative proportion of labeled boutons in each area was expressed as a percentage of all boutons mapped in the rhinal cortices for each injection site. The relative laminar proportion of small and large boutons in each layer was expressed as a percentage of the total number of boutons within each laminar group, in each area, for each injection site. Relative proportions within areas 28, 35, and 36 were subsequently collapsed to express an omnibus relative laminar density for the superficial and deep layers of the rhinal cortices. This was expressed as the percentage of small and large boutons within the superficial (I–III) or deep (IV–VI) layers for each injection and then averaged across cases. Numerical data were transferred to a database (Microsoft Excel).

Correlated light microscope / EM analyses

We used a combined light microscope / EM approach to study synapses of the ACC and pOFC-rhinal pathways (e.g., Barbas et al., 2003; Medalla and Barbas, 2010). Briefly, after tissue processing to view tracer label we mounted on glass slides brain sections with labeled axon boutons in the areas of interest, viewed them while wet, captured images of labeled sites with a CCD camera, and cut small blocks of tissue containing label, osmicated, and embedded them for ultrathin sectioning. We then cut the blocks of tissue into ultrathin sections (Ultracut, Leica, Wetzlar, Germany) in series to reconstruct labeled synapses, as described briefly below and in previous studies (e.g., Germuska et al.,

2006; Medalla et al., 2007; Zikopoulos and Barbas, 2007; Bunce and Barbas, 2011).

We viewed fields with labeled boutons in the EM (100CX, JEOL, Peabody, MA) and captured images using a digital camera (ES1000W, Gatan, Pleasanton, CA) at a magnification of 6,000–33,000×. We determined synapse type and measured synapses from the images using image analysis systems (ImageJ; Reconstruct, Fiala, 2005). For serial reconstruction, we first aligned images to correct misalignment caused by serial sectioning and imaging of the tissue and used the software to apply transformations expressed explicitly as a set of rotations, scaling, and stretches, or implicitly by specifying a set of corresponding points in contiguous images. The points were then aligned using a selection of linear and nonlinear transformations. To ensure that the generated 3D object was geometrically accurate, the dimensions of each serial image were calibrated. We traced pre- and postsynaptic elements and generated a 3D reconstruction of an object represented in the aligned image sections. The boundaries of an object were defined by contours for each section. Once all object contours were defined in serial sections the program generated a 3D Virtual Reality Modeling Language object.

Confocal imaging

We used a Revolution dual spinning disk (DSD) white light confocal microscopy system to image fluorescence signal (Andor, Belfast, UK). The DSD system was composed of an AMH-200-F6S white light source and a Clara Interline CCD camera attached to an Olympus BX63 microscope with a motorized reflected fluorescence system (model BX3-RFAA) and a motorized stage (model V31XYZE, Prior Scientific, Rockland, MA) controlled by an Olympus BX3-CBH U-MCZ controller box. Stacks of images were captured using 60× or 100× oil immersion objectives (Olympus), with MetaMorph NX software on a Dell Precision T3520 Workstation running Microsoft Windows 7 (32 bit). Filters specific to the wavelength of the distinct fluorophores were used to image separate channels which were captured individually and compiled into composite stacks using Fiji (Schindelin et al., 2012) and then imported into Reconstruct for scaling, and quantification of boutons in apposition to inhibitory postsynaptic targets. Stacks were captured at 0.1 μm z-intervals in the upper and deep layers of rhinal areas 28, 35, and 36.

Quantitative analysis of labeled synapses: fluorescent signal

We used correlated light-fluorescence microscopy combined with immunohistochemistry to label postsynaptic

sites. Data derived from the light microscope-guided subsequent analysis at the fluorescence microscope. We employed triple labeling to view the tracer and two classes of inhibitory neurons expressing PV, CB, or CR. Boutons in apposition to inhibitory postsynaptic targets were quantified by manually searching through the stacks. We normalized the percentage of boutons in apposition to inhibitory postsynaptic targets to account for differences in signal density. We divided the number of boutons apposed to each calcium-binding protein immunoreactive target (CB, CR, PV) by the total number of axon boutons counted within the lamina within each area. This value was then divided by the quotient of the volume of the area sampled for each calcium-binding protein divided by the volume of the sampled layers. These percentages were then averaged across cases.

Quantitative analysis of labeled synapses: EM

Images of sites containing labeled synapses were imported in Reconstruct to mark synapses by type, cross-sectional area and synaptic length (e.g., Barbas et al., 2003; Germuska et al., 2006). We used classical criteria for identifying synapses and profiles (Peters et al., 1991; Peters and Palay, 1996; Carr and Sesack, 1998): by the aggregation of synaptic vesicles in the presynaptic bouton; rigid apposition of the presynaptic and postsynaptic membranes and widening of the extracellular space and the presence of pre- and post-synaptic membrane specializations. Asymmetric synapses (type I) have thickened postsynaptic densities and rounded vesicles; symmetric (type II) synapses have thin postsynaptic densities and pleomorphic vesicles. Pyramidal neurons have dendrites with spines, which receive the vast majority of synapses. Inhibitory neurons in the cortex have smooth or sparsely spiny dendrites and receive synapses mostly on the shafts of their dendrites. Inhibitory neurons form symmetric synapses with a variety of elements from other neurons. Axon terminals are >0.1 μm in diameter and contain synaptic vesicles, and often have mitochondria. Dendritic shafts contain mitochondria, microtubules, and/or rough endoplasmic reticulum, while dendritic spines lack these organelles.

2D and 3D EM analysis

For 2D analysis at the EM we exhaustively sampled all labeled boutons from series of sections. We used ImageJ or Reconstruct to measure the major diameter of labeled boutons at the level of the synapse. For 3D analysis, we used series of 100 sections and identified all labeled boutons in the series. We followed each bouton throughout adjacent serial sections (15–180 sections) for each synapse and reconstructed labeled

boutons and their postsynaptic targets using the program Reconstruct. We traced pre- and postsynaptic elements and generated a 3D reconstruction of an object represented in the aligned image sections. The boundaries of an object were defined by contours for each section. Once all object contours were defined in serial sections, the program generated a 3D Virtual Reality Modeling Language object.

Statistics

Datasets were compared using analysis of variance (ANOVA), analysis of covariance (ANCOVA) with post-hoc comparisons made using Fisher's least significant difference using PASW Statistics (v. 18) or Statistica (v. 11) for Windows. To test the reliability of the sampling method we examined if the proportion of total boutons sampled in the superficial and deep layers of each area of interest fell within $\sim$10% of the proportions calculated during exhaustive sampling and stereological quantification (data not shown). All error values are reported as standard error of the mean (SEM) unless otherwise noted.

Photography

Photomicrographs were captured using a CCD camera mounted on an Olympus Optical microscope (BX60) connected to a personal computer using a commercial imaging system (NeuroLucida, Virtual Slice software, MicroBrightField) or using a digital camera (ES1000W, Gatan) at the EM. For the population analysis, we acquired image stacks of several focal planes in each area of interest, resulting in pictures with high depth of field focused throughout the z-axis extent. Stacks were then combined to create a composite image using ImageJ, scaled, and all labeled boutons were traced. ImageJ output was exported to a database in Excel. For presentation, images were imported into Adobe Photoshop CS5 (San Jose, CA) for adjustment of overall brightness and contrast but were not retouched. Images were assembled in ACD Canvas X or Adobe Illustrator CS5.

RESULTS

Nomenclature

The nomenclature used is based on previous maps for the rhinal region (Suzuki and Amaral, 1994b) as used in our previous studies (Rempel-Clower and Barbas, 2000; Hoistad and Barbas, 2008). Our analysis in the medial temporal lobe included the entorhinal (area 28) and perirhinal (areas 35 and 36) cortices using cytoarchitectonic borders to demarcate areas and layers consistent with previous maps (Amaral et al.,

1987; Suzuki and Amaral, 1994a; Insausti and Amaral, 2008). The term rhinal refers to all three areas for brevity. Delineation of the architectonic borders of orbitofrontal and anterior cingulate areas is according to the map of Barbas and Pandya (1989), modified from the classic map of Walker (1940) and subsequently supported by quantitative architectonic criteria (Dombrowski et al., 2001). Area 13 occupies an intermediate position between the caudally situated areas OPro and OPAll, on the one hand, and the rostrally situated area 11, on the other hand (Barbas and Zikopoulos, 2006). Both posterior areas 13 and OPro are dysgranular, with an incipient granular layer 4. Area 13 and OPro are incorporated into area OFdg in the map of Morecraft et al. (1992). Area 13 (Barbas and Pandya, 1989) is largely coextensive with areas 13b, 13m, 13l (Carmichael and Price, 1994). Area OPro (Barbas and Pandya, 1989) partially corresponds to orbital areas assigned to the insula as Iai, Ial, Iapl (Carmichael and Price, 1994).

Injection sites

Data were obtained from injections of BDA, LY, or FE in area 32 ($n = 6$ injection sites in five cases) and CBl or LY in OPro/posterior area 13 ($n = 3$ cases; Table 1). In all cases the tracer occupied all cortical layers. In three cases the injection impinged on adjacent cortices. In case AY the corona of the injection impinged on the medial part of area 9. Rhinal cortices have few, if any, connections with the medial portions of area 9 (Insausti et al., 1987; Barbas et al., 1999; Kondo et al., 2005), suggesting that this region did not contribute significantly to axon terminations seen in areas 28 and 35. In case BN, the injection was in caudal area 32, with partial involvement of rostral area 24, a region considered part of the ACC, and which is reported to have some connections with rhinal cortices as well (Insausti et al., 1987; Insausti and Amaral, 2008). Finally, in case BI-L the core of the injection was in posterior area 13 with some halo in area OPro.

Topography of ACC and pOFC terminations in the rhinal cortices

Initial observations revealed labeled *terminaux* and *en passant* boutons present in the superficial (I–III) and deep (IV–VI) layers of the rhinal cortices (Fig. 1B,C). Labeled axons from ACC and pOFC were distributed throughout the anterior–posterior extent of the rhinal cortices. Figures 2 and 3 show the areal and laminar distribution of ACC and pOFC terminations in the superficial (I–III) and deep (IV–VI) layers in areas 28, 35, and 36, obtained with the use of exhaustive sampling and unbiased stereological techniques. The ACC and pOFC

pathways diverged into largely separate zones in the rhinal cortices. The ACC terminations were most dense in areas 28 and 35 (area 28 = 75.6 ± 14.4%; area 35 = 22.7 ± 13.6%) and sparse in area 36 (1.7 ± 2.0%; Fig. 4A). In contrast, pOFC terminals were largely found in area 36 (90.1 ± 1.0% [sd]) while fewer terminations were observed in areas 28 and 35 (1.0 ± 0.1% [sd]; 9.2 ± 1.0% [sd], respectively; Fig. 4B). These findings show that the ACC and pOFC terminate largely in complementary sectors of rhinal cortex.

We collapsed data on axon terminations to areas 28 and 35 for each pathway and analyzed the laminar distributions of boutons in the upper and deep layers of the rhinal cortices. Terminations from ACC axons were evenly distributed in the superficial (50.7 ± 24.1%) and deep layers (49.3 ± 24.1%; black bars in Fig. 4C), as was the case for terminations from the pOFC (OPro and posterior area 13; upper = 47 ± 5.9% [sd]; deep = 53 ± 5.9% [sd]; black bars in Fig. 4D). In general, the overall pattern of terminations from the ACC and pOFC to the rhinal cortices confirms and extends previous findings (Van Hoesen et al., 1975; Carmichael and Price, 1995; Kondo et al., 2005; Insausti and Amaral, 2008; Saleem et al., 2008). The near even laminar distribution of boutons in the upper and deep layers by both pathways shown quantitatively suggests that the ACC directly and the pOFC indirectly impinge on rhinal layers that send input as well as receive the output of the hippocampus.

Presynaptic size of prefrontal terminations in the rhinal cortices: light microscope analysis

We next analyzed the size of axon terminals in the medial temporal lobe. The rationale for measuring bouton size is based on anatomic, physiologic, and computational studies which have shown that large boutons have more synaptic vesicles and greater synaptic efficacy, because of increased probability of neurotransmitter release and increased likelihood of multivesicular release with each action potential (Tong and Jahr, 1994; Rosenmund and Stevens, 1996; Murthy et al., 1997; Walmsley et al., 1998; Stevens, 2003; Germuska et al., 2006; Zikopoulos and Barbas, 2007). Analysis of the size (major diameter) of anterogradely labeled boutons from the ACC in area 28 ($n = 4{,}449$) and area 35 ($n = 5{,}591$), and from pOFC to area 36 ($n = 4{,}215$) showed that the majority of boutons from both pathways fell between 0.5–1.5 μm in diameter (Fig. 5A,B). A k-means cluster analysis (PASW Statistics 18) sorted terminations into small and large populations based on the major diameters of boutons. Initial cluster analysis
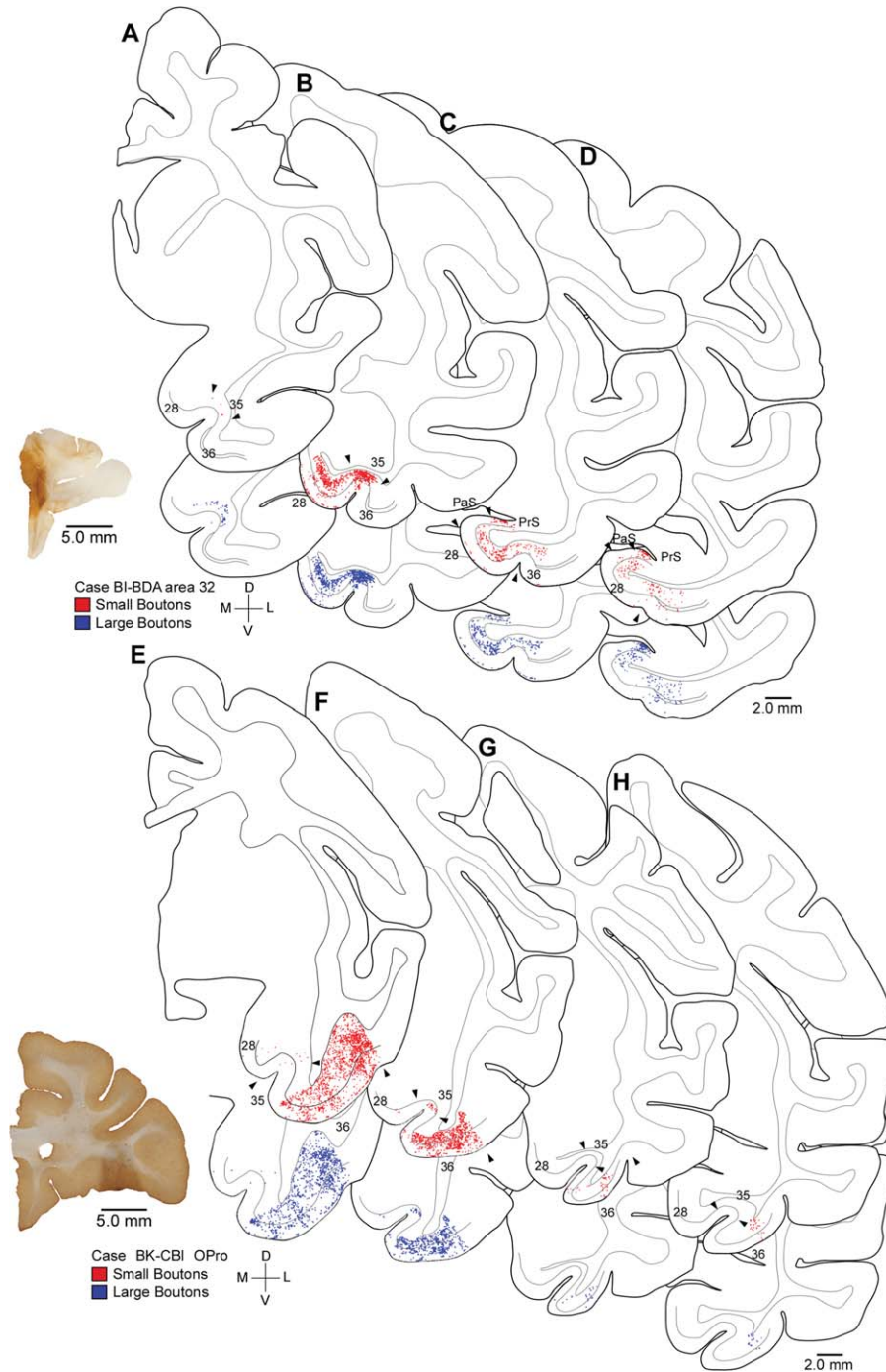
Figure 2. Distribution of terminations from ACC and pOFC in the rhinal cortices. Rostral **(A,E)** through caudal **(D,H)** tracings of coronal sections through the rhinal cortices (areas 28, 35, and 36) show the areal and laminar distribution of small (red) and large (blue) labeled boutons following injection of the anterograde tracer BDA in ACC area 32 **(A–D)** or CBI in OPro **(E–H)**. Anterograde tracer injection sites are shown on coronal sections (bottom left). Lines through the middle of the cortex denote layer IV. BDA, biotinylated dextran amine; CBI, cascade blue.

from the individual cases showed no significant differences for major diameter of boutons for individual cases or layers (ANOVA, $F < 1.0$; $P > 0.05$; data not shown), so we pooled data and performed an overall cluster analysis on the ACC pathways to area 28 and 35 individually. Analysis by area showed that small ACC terminations in both the entorhinal (area 28) and adjacent area 35, centered around 0.8 µm (SEM $\pm$ 0.004) and large boutons centered around 1.5 µm (SEM $\pm$ 0.007; area 28 = $F[1,4447] = 8,416.4$, $P < 0.001$;
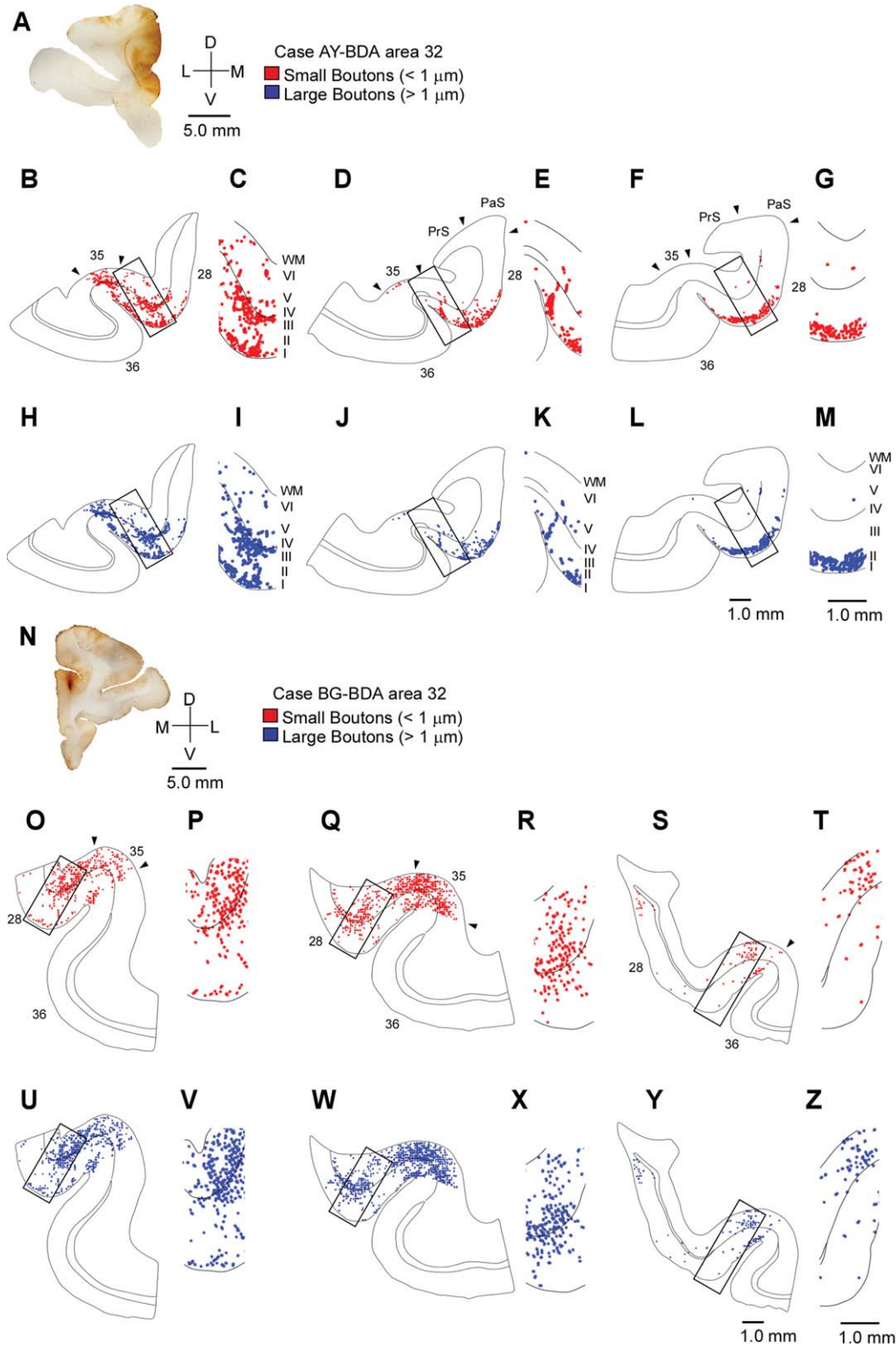
Figure 3. Distribution of terminations from ACC to the rhinal cortices. **A:** Injection site in ACC area 32, with spread to medial area 9 (above). **B–M:** Rostral (B,H) through caudal (G,M) tracings of coronal sections through the rhinal areas show the areal and laminar distribution of small (red) and large (blue) labeled boutons in areas 28, 35, and 36 (A, case AY). Higher-magnification insets show the laminar distribution of terminations. **O–Z:** Rostral through caudal tracings of coronal sections show small (O–T) and large (U–Z) boutons in the rhinal cortices in a case with a small BDA injection in area 32 (N, top case BG). WM, white matter.
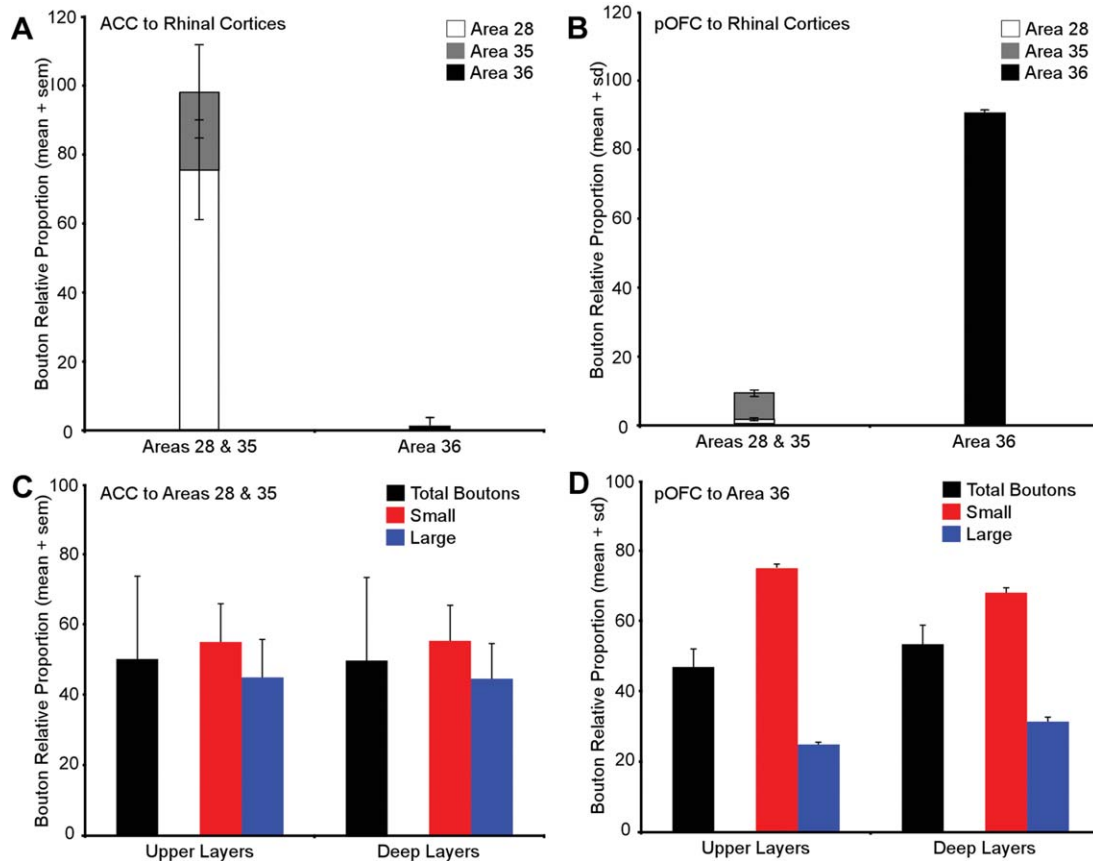
Figure 4. Comparison of areal and laminar distribution of ACC and pOFC terminations in the rhinal cortices. **A:** Relative proportions of labeled axon boutons from the ACC were densest in the rhinal areas 28 and 35, and sparse in area 36. **B:** The highest relative proportion of labeled boutons from pOFC axons was in area 36, but few terminations were observed in areas 28 and 35. **C:** Relative proportions of labeled ACC boutons collapsed across rhinal areas 28 and 35. The ratio of large to small boutons approached 50:50 in the superficial and deep layers of rhinal areas 28 and 35 following 2D analysis at the light microscope. **D:** The ratio of large to small boutons originating from pOFC axons was close to 30:70 in both the upper and deep layers of rhinal area 36. ACC, anterior cingulate cortex; pOFC, posterior orbitofrontal cortex.

area 35 = F[1,5589] = 9474.1; $P < 0.001$). An omnibus cluster analysis of the collapsed data showed that overall small boutons centered at 0.8 μm (SEM ± 0.002) and the large at 1.5 μm (SEM ± 0.005); F[1,10038] = 17849.1, $P < 0.001$, Fig. 5C). Similar values were obtained for the pOFC pathway (small boutons centered at 0.8 μm, SEM ± 0.003; large boutons centered around 1.45 mm, SEM ± 0.009; F(1,4213) = 7493.3; $P < 0.001$; Fig. 5C). The overall bouton major diameter population mean was 1.0 μm for both the ACC and pOFC pathways and their normalized frequency distributions were nearly identical (Fig. 5D).

The cluster analysis yielded a criterion threshold of 1.1 μm for both pathways, which was used to classify boutons into small (≤1.1 μm) and large (>1.1 μm) populations. Using this criterion we found that the proportion of small to large ACC boutons in rhinal areas 28 and 35 approached 50:50 in both the upper (small = 55.1 ± 10.9%; large = 44.9 ± 10.9%) and deep layers (small =

55.4 ± 10.1%; 44.6 ± 10.1%; Fig. 4C). In sharp contrast, pOFC innervated area 36 predominantly through small boutons (upper layers, small = 75.2 ± 1.2% [sd]; large = 24.8 ± 1.2% [sd]; deep layers, small = 68.4 ± 1.2% [sd]; large = 31.6 ± 1.2% [sd]; Fig. 4D).

ACC and pOFC pathways target distinct inhibitory mechanisms in the rhinal cortices

We next investigated the excitatory and inhibitory nature of postsynaptic targets of prefrontal pathways in the rhinal cortices. The density of GABAergic neurons is greater in the upper layers of the entorhinal cortex compared to the deep layers (Jongen-Relo et al., 1999). In the primate cortex, these GABAergic neurons are segregated into three largely nonoverlapping neurochemical classes of inhibitory neurons, distinguished by their expression of parvalbumin (PV), calbindin (CB) or calretinin (CR; DeFelipe et al., 1989b; Hendry et al.,
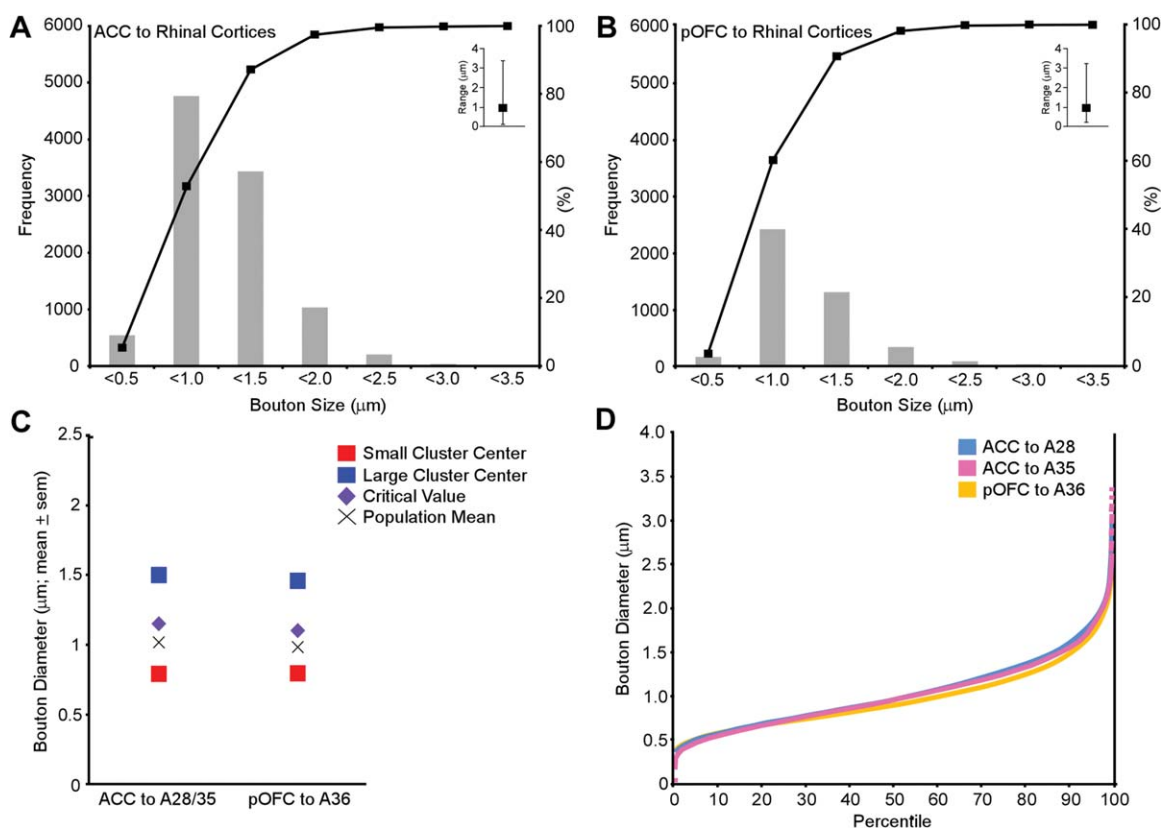
Figure 5. Presynaptic characteristics of ACC (area 32) and pOFC (area OPro) terminals in the rhinal cortices. Light microscope analysis: **A:** Bouton major diameter frequency distributions in the rhinal cortices following BDA injection in ACC area 32. **B:** following injection of CBl in area OPro. Insets show the range of the distributions. **C:** Comparison of bouton major diameter clusters in areas 28/35 and area 36 in the two pathways following 2D analysis at the light microscope. The average major diameter for distributions in the superficial and deep layers was 1.0 μm for both pathways (denoted by X). The critical value for placement within the large cluster was >1.1 μm for both pathways (denoted by purple diamond). **D:** Normalized frequency distributions of bouton major diameters in the rhinal cortices following anterograde tracer injections in ACC and pOFC.

1989). The CB and PV neurons are concentrated in the upper and middle rhinal cortical layers and both classes predominantly target principal cells (DeFelipe et al., 1989a; Pitkanen and Amaral, 1993; Mikkonen et al., 1997; reviewed by Somogyi et al., 1998). The majority of CR neurons are found in superficial cortical layers, but their pattern of innervation of nearby neurons is more complex. There is evidence that in the upper layers CR inhibitory neurons form synapses with other inhibitory neurons and thus disinhibit the local network of several areas including the primary visual cortex (area 17), the anterior cingulate cortex (areas 24, 25, and 32), and dorsolateral prefrontal cortex (area 9) in macaques and the temporal cortex (areas 38, 21, and 20) in humans (Gabbott and Bacon, 1996; DeFelipe, 1997; del Rio and DeFelipe, 1997; Meskenaite, 1997; Melchitzky et al., 2005).

We first investigated the postsynaptic targets of ACC and pOFC pathways in the rhinal cortices to determine the proportion of boutons in apposition with inhibitory neurons in rhinal areas 28, 35, and 36. On average 23% of boutons from the ACC were in apposition with inhibitory postsynaptic elements (24.7% in the upper layers, 17.8% in the deep layers; $n = 1,199$ labeled boutons in areas 28 and 35; $n = 664$ boutons in the upper layers; $n = 535$ boutons in the deep layers; examples in Fig. 6A–C,E–G). The rest of the labeled boutons from ACC (~77%) were not apposed to labeled inhibitory structures and, therefore, likely form synapses with unlabeled dendritic spines of excitatory pyramidal neurons. In the pOFC pathway to area 36,17% of the boutons were in apposition to inhibitory targets (19.5% in the upper layers; 14.6% in the deep layers; $n = 5,507$ labeled boutons in area 36; $n = 2,406$ in the upper layers; $n = 3,101$ boutons in the deep layers; examples in Fig. 6D,H). In this pathway ~83% of the labeled terminals likely formed synapses with unlabeled dendritic spines of excitatory pyramidal neurons.

Boutons from ACC axons in the upper layers of areas 28 and 35 were found to be in apposition to

postsynaptic targets labeled with CR (15.6 ± 1.9%) significantly more than those expressing PV (3.6 ± 2.5%) or CB (5.5 ± 3.5%; $P < 0.001$). In the deep layers of areas 28 and 35, ACC boutons were most frequently apposed to PV labeled postsynaptic sites (8.1 ± 0.3%), followed by sites labeled for CR (5.2 ± 1.2%) and CB
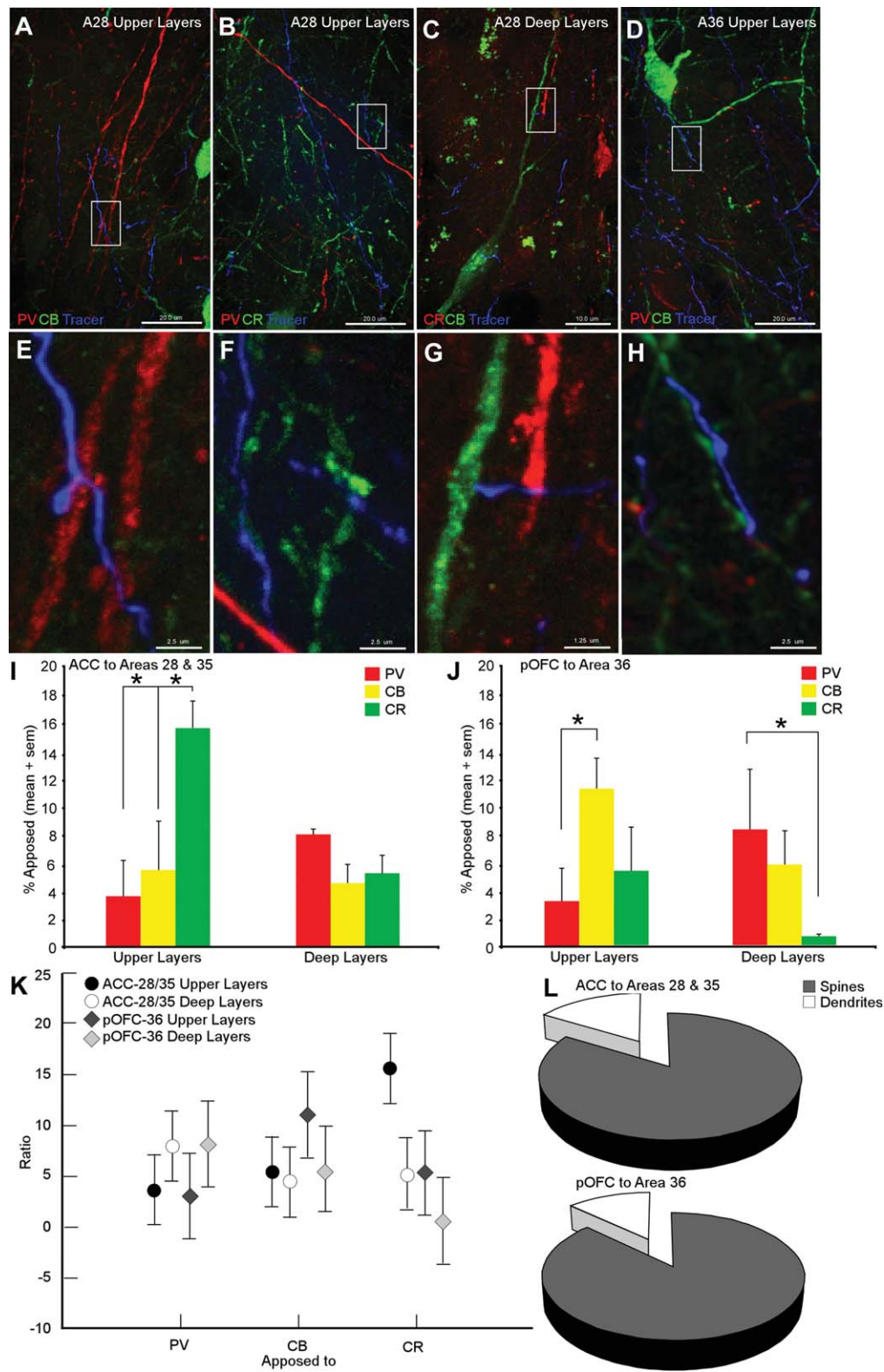

Figure 6.

(4.5 ± 1.4%; Fig. 6I,K). A similar pattern was seen in the deep layers of rhinal area 36, for boutons from pOFC axons which were also more frequently apposed to PV dendritic sites (8.2 ± 4.3% [sd]; CB: 5.7 ± 2.4% [sd]; CR: 1.0 ± 0.1% [sd]; $P < 0.001$; Fig. 6J,K). This pattern was different for the pathway from the pOFC to the upper layers of area 36, where most appositions were found with postsynaptic dendritic sites labeled for CB (11.1 ± 2.2% [sd]) than PV (3.1 ± 2.4% [sd]; $P < 0.001$) or CR (5.3 ± 3.1% [sd]). Focusing exclusively on inhibitory postsynaptic targets, ACC boutons in the upper layers of rhinal areas 28 and 35 were predominantly apposed to CR dendrites (69.4 ± 19.0%) followed by CB (18.3 ± 11.3%) and PV (12.3 ± 9.0%). In the deep layers ACC boutons were most frequently apposed to PV (35.3 ± 5.6%) followed by CR (29.4 ± 5.2%) and CB (24.7 ± 7.0%) targets. Boutons from pOFC in the upper layers of area 36 were mostly apposed to CB dendrites (59.4 ± 12.2%) followed by CR (26.1 ± 5.7%) and PV (14.6 ± 6.5%) postsynaptic sites. In the deep layers, similar to the ACC pathway, pOFC boutons were most frequently apposed to PV (55.4 ± 4.6%) followed by CB (39.6 ± 1.3%) and CR (5.2 ± 3.2%). These results show that the ACC and pOFC target distinct inhibitory mechanisms in the upper layers of their preferred areas of termination within the rhinal cortices.

Synaptic characteristics of ACC and pOFC terminations in the rhinal cortices: EM analysis

We next investigated interactions between the ACC and pOFC pathways in the rhinal cortices at the ultrastructural level to characterize the pre- and postsynaptic targets of the circuit for a subset of tissue labeled for tracer as well as for PV and CB ($n = 41$ labeled ACC boutons in areas 28 and 35, which formed 43 synapses: upper layer: $n = 38$; deep layers: $n = 3$). All boutons formed asymmetric synapses which were presumed to be excitatory, and of these some were perfo-

rated (9%). Similarly, in the pOFC pathway labeled boutons formed asymmetric synapses in area 36 ($n = 39$ boutons, which formed 48 synapses: upper layers: $n = 18$; deep layers: $n = 21$). All boutons from pOFC formed asymmetric synapses and were presumed to be excitatory. Equal numbers of boutons were *terminaux* and *en passant* and a third of them formed perforated synapses.

Initially we performed a 2D analysis on the diameters of ACC and pOFC boutons and found that they were comparable regardless of layer innervated (ACC: overall = 1.1 ± 0.07 μm; upper layers = 1.1 ± 0.06 μm; deep layers 1.2 ± 0.6 μm; pOFC overall = 1.0 ± 0.04 μm; upper layers = 1.0 ± 0.09 μm; deep layers = 1.0 ± 0.05 μm). Using the criterion threshold calculated for the 2D population analysis at the light microscope (1.1 μm), the proportion of small to large ACC boutons approached 50:50 (small = 53.7%; large = 46.3%). In contrast, in the pOFC pathway small boutons predominated (small = 67.6%; large = 32.4%). In both pathways, the distribution of small and large boutons was comparable in the upper and deep layers of the rhinal cortices, consistent with our findings at the light microscope (ACC upper: small = 51.2%; large = 48.7%; ACC deep: small = 66.7%; large = 33.3%; pOFC upper: small = 61.1%; large = 38.9%; pOFC deep = small = 73.7%; large = 26.3%; compare with light microscope data in Fig. 4C).

We then performed a 3D EM analysis on boutons for both pathways (ACC $n = 19$ labeled boutons, forming 22 synapses; pOFC $n = 39$ labeled boutons forming 48 synapses in area 36). Bouton volumes were identical across pathways (ACC = 0.25 ± 0.04 μm^3; pOFC = 0.25 ± 0.05 μm^3). In both pathways, bouton volume was positively correlated with the size of the synapse (ACC synapse area = 0.23 μm^2; R = 0.60, $P = 0.01$; pOFC synapse area = 0.19 μm^2; R = 0.63, $P = 0.01$). In both pathways, the majority of synapses were made with unlabeled spines of putative excitatory neurons, although a significant number of synapses were made with postsynaptic targets of presumed inhibitory neurons (ACC: spines = 83.7%; dendritic shafts = 16.3%;

Figure 6. Inhibitory postsynaptic targets of the ACC and pOFC pathways to the rhinal cortices. **A–D:** Examples of ACC (A–C) and pOFC (D) boutons in apposition with inhibitory neurons in the rhinal cortices. A: ACC bouton (blue) in apposition with a PV positive dendrite (red) in the upper layers of area 28. B: ACC bouton (blue) in apposition with a CR dendrite (green) in the upper layers of area 28. C: ACC bouton (blue) in apposition to a CR dendrite (red) in the deep layers of area 28. D: pOFC boutons forming two appositions on a CB dendrite (green) in the upper layers of area 36. The white rectangles in (A–D) show the location of the higher magnification images presented in **E–H**. **I**: Relative proportion of ACC boutons in apposition to PV, CB, and CR postsynaptic targets in the upper and deep layers of the rhinal areas (collapsed across areas 28 and 35). **J**: Relative proportion of pOFC boutons in apposition to PV, CB, and CR postsynaptic targets in rhinal area 36. **K**: Ratio of pathways apposed to specific inhibitory targets in the rhinal cortices. Vertical bars denote 0.95 confidence intervals. **L:** Analysis at the EM showed that both the ACC and pOFC pathways formed synapses with a similar percentage of inhibitory targets in the rhinal cortices. Tracer channel is pseudocolor. ACC, anterior cingulate cortex; CB, calbindin; CR, calretinin; PV, parvalbumin; pOFC, posterior orbitofrontal cortex.
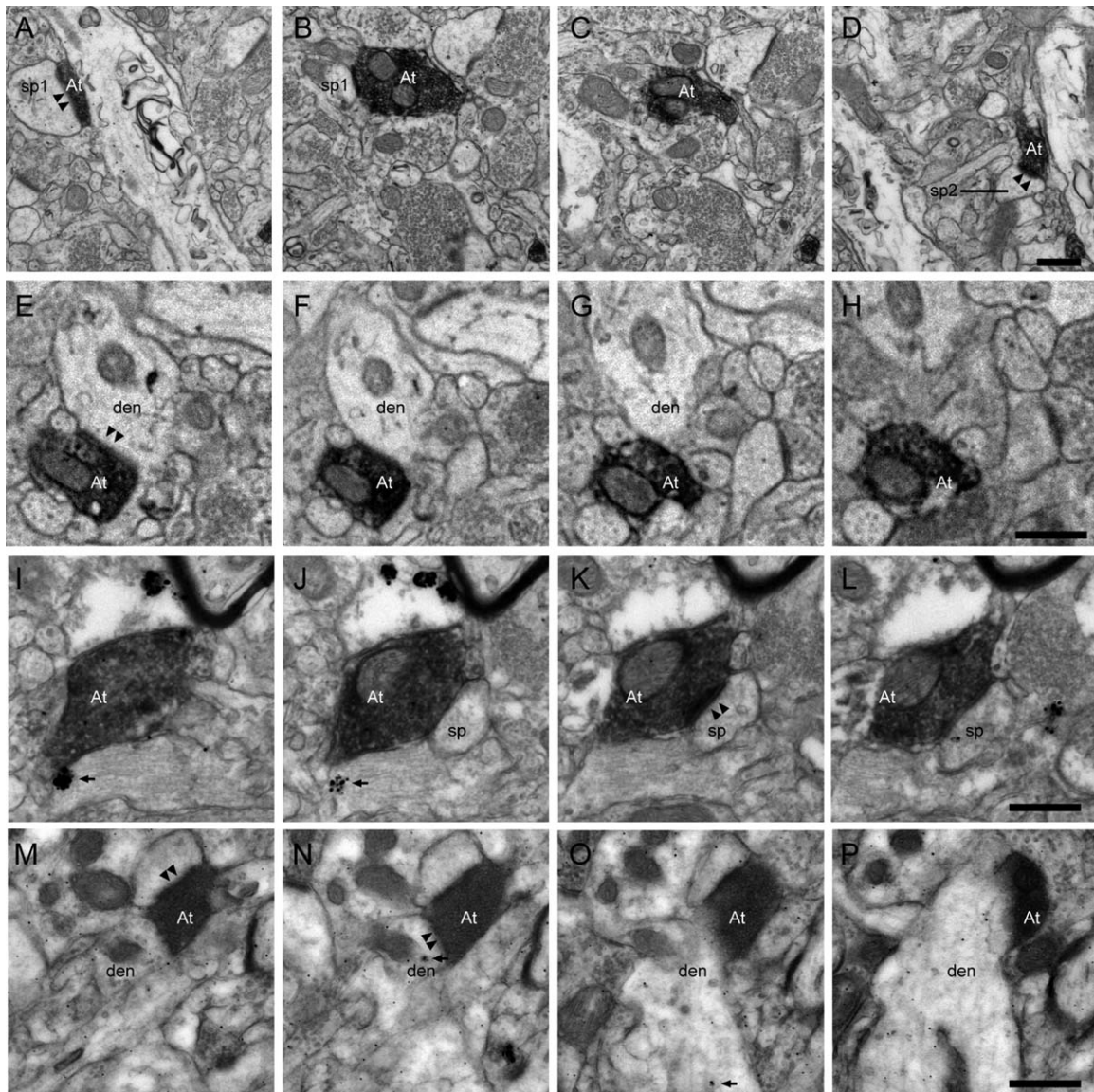
Figure 7. Examples of prefrontal terminals forming synapses with excitatory and inhibitory neurons in the rhinal cortices. **A–D:** Serial ultrathin sections show a multisynaptic ACC bouton (At) forming synapses with two distinct unlabeled spines (sp1, sp2, arrowheads denote postsynaptic density [psd]) in the upper layers of area 28. **E–H:** Serial ultrathin sections show an ACC bouton (At) forming a synapse with an unlabeled dendrite (den) in the upper layers of area 28 (arrowheads denote psd). **I–L:** Serial ultrathin sections show a labeled ACC terminal (At) forming a synapse with a spine (sp) emanating from a PV-positive dendrite in the upper layers of area 28 (arrowheads denote psd). Note the gold signal in I,J denoting immunoreaction for PV (arrow). **M–P:** Serial ultrathin sections show a labeled pOFC bouton (At) forming multiple synapses with a spine (sp) and a CB expressing dendrite (den) in the upper layers of area 36. Note the gold signal in N,O denoting CB immunoreaction (arrow). Scale bars = 0.5 μm.

pOFC: spines = 87.5%; dendritic shafts = 12.5%; Figs. 6L, 7). In both pathways, the proportion of inhibitory postsynaptic targets was within the range of that observed at the fluorescence microscope (ACC boutons in apposition to inhibitory targets = 23%; pOFC boutons in apposition to inhibitory targets = 17%). Putative inhibitory postsynaptic targets were identified by morphological characteristics or neurochemical staining against CB or PV (Fig. 7).

DISCUSSION

Posterior orbitofrontal and anterior cingulate regions have largely divergent projections to medial temporal cortices that are strongly linked with the hippocampus. Using multiple approaches from the system to the synapse, we found that pathways from pOFC terminated largely in area 36, while ACC pathways innervated most robustly the entorhinal cortex (area 28) and adjacent area 35. This pattern of innervation of medial temporal

cortices by prefrontal pathways confirms and extends previous findings (Van Hoesen et al., 1975; Carmichael and Price, 1995; Kondo et al., 2003, 2005; Saleem et al., 2008). It should be noted that the divergence of the two prefrontal pathways is not complete. Previous findings have shown that the most caudal part of pOFC has a significant projection to the entorhinal cortex as well (Rempel-Clower and Barbas, 2000; Insausti and Amaral, 2008).

In addition, our findings showed that the two prefrontal pathways innervated the upper and deep layers of medial temporal cortices, consistent with previous studies that reported robust prefrontal terminations in all layers of rhinal cortex, or with slight preference for the deep layers in moderately targeted regions (Rempel-Clower and Barbas, 2000; Insausti and Amaral, 2008). This evidence suggests that the two prefrontal pathways exert a strong influence on the input to the hippocampus through the upper layers, as well as the output of the hippocampus through the deep layers. Thus, while the hippocampus issues strong direct projections to the medial and to a lesser extent the orbital prefrontal cortices, the ACC and pOFC pathways are positioned to indirectly impinge on hippocampal signals via the rhinal cortices.

The regionally biased termination by pOFC and ACC in medial temporal cortices was only one of the features that distinguished the two pathways. Further, the pOFC pathway to medial temporal cortex terminated predominantly as small boutons, which form small synapses. By contrast, nearly half of the boutons from ACC axons were large, which form large and efficient synapses (for discussion, see Germuska et al., 2006). In this regard, the ACC may act as a "driver" of information in the rhinal cortices, similar to the projections to parahippocampal and temporal auditory cortices (Medalla et al., 2007; Bunce and Barbas, 2011; Barbas et al., 2013).

Another novel finding was the relationship of the pOFC and ACC pathways with different classes of inhibitory neurons, which play a critical role in generating synchronous oscillatory activity in neural networks (Markram et al., 2004; Isaacson and Scanziani, 2011). Importantly, prefrontal attentional signals evoke synchronous neural activity across distributed cortical areas and can mediate preferred frequency domains in segregated layers within a given area (Womelsdorf and Fries, 2007; Borgers et al., 2008; Ainsworth et al., 2011, 2012; Buffalo et al., 2011). Layer-specific oscillatory activity in a number of frequency bands, including theta (4–8 Hz), alpha (8–12 Hz), beta (12–30 Hz), and gamma (30–100 Hz), are thought to underlie rhinal cortico-cortical and cortico-hippocampal processing and
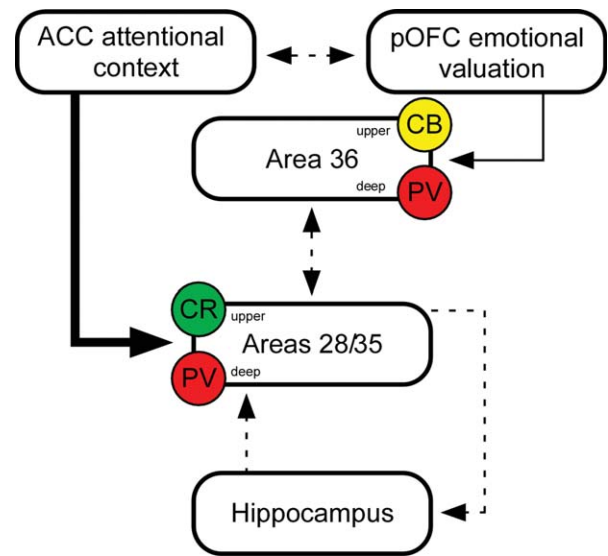

Figure 8. Summary of the presynaptic and the subset of inhibitory postsynaptic characteristics of the ACC and pOFC pathways to areas 28, 35, and 36 of the rhinal cortices. Both pathways innervate mostly excitatory neurons (not shown) as well as a significant proportion of distinct neurochemical classes of inhibitory neurons, as shown here. Dotted lines show known circuits from other studies. The size of lines and arrows from ACC and pOFC reflects the size of synapses. ACC signals, via a greater proportion of large and synaptically efficient boutons on excitatory neurons (not shown) also impinge on CR (green) inhibitory neurons in the upper layers of areas 28 and 35 where they are positioned to disinhibit the neurons which originate the principal cortical input to the hippocampus. ACC signals arriving in the deep layers target PV (red) inhibitory neurons that may modulate hippocampal output to allow transfer of signals from the deep layers to other cortices or to reenter the cortico-hippocampal loop via ascending projections to area 28. Signals from the pOFC target CB (yellow) inhibitory neurons in the upper layers of area 36, which may modulate the integration of sensory valuation signals, and project to areas 28 and 35. Similar to the ACC pathway to rhinal deep layers, pOFC projections to the deep layers of area 36 target PV neurons where they may enhance inhibition in the cortical circuit leading to other cortices.

are correlated with memory performance in monkeys and humans (Fell et al., 2001; Sederberg et al., 2003; Canolty et al., 2006; Jutras et al., 2009; reviewed in Jutras and Buffalo, 2010; Fell et al., 2011). The significance of specialized interactions of prefrontal pathways with layer-specific inhibitory mechanisms in the rhinal cortices stems from the laminar segregation of input (upper layers) and output (deep layers) zones, to and from the hippocampus, as elaborated below (Fig. 8).

Prefrontal cortices may facilitate passage of signals to the hippocampus

Transmission of signals from the upper layers of the rhinal cortices to the hippocampus is not always

assured, but is gated by inhibitory neurons. In the primate cortex, inhibitory control is largely exercised through feedforward excitatory (glutamatergic) projections acting on local inhibitory neurons, and rarely through inter-areal projections of inhibitory neurons (Tomioka and Rockland, 2007). Previous work in guinea pigs has shown that ~15% of boutons from medial prefrontal axons to rhinal cortices form synapses with GABAergic dendritic profiles (Apergis-Schoute et al., 2006), in a range similar to our findings.

Further, the present findings show that the pOFC and ACC differed in their preferred innervation of inhibitory neurons. The predominant association of the pOFC pathway was with CB neurons. The pOFC, like area 36, is a multimodal region, innervated by a host of sensory-specific cortices and limbic cortices associated with the internal status of the environment of motives and drives (reviewed in Barbas, 1995, 2000a,b; Barbas et al., 2011). Previous studies have suggested that the pOFC-area 36 interaction underlies the integration of perceptual, emotional valuation, and mnemonic signals to gauge expected rewards (Suzuki, 2010; Clark et al., 2012, 2013; Ohyama et al., 2012). Our findings suggest that the pOFC is poised to modulate perceptual signals in area 36, by targeting CB neurons. The neurochemical class of CB inhibitory neurons innervate the distal dendrites of nearby pyramidal neurons and are thought to increase the signal-to-noise ratio between relevant signals and distracters (Wang et al., 2004; Zaitsev et al., 2005; Medalla and Barbas, 2009; 2010). The product of this integration can then be applied to the input and output of areas 35 and 28.

In contrast, terminations from ACC axons in the upper layers of areas 28 and 35 were most frequently found in apposition with CR positive dendrites. In the upper cortical layers, CR neurons innervate other inhibitory neurons in several cortical areas (e.g., Gabbott and Bacon, 1996; Melchitzky et al., 2005), and effectively disinhibit neighboring excitatory neurons. In combination with a robust excitatory projection through large and efficient synapses on excitatory neurons in entorhinal cortex, the ACC is poised to transmit to the hippocampus signals that converge on medial temporal cortices. The ACC is thought to have a role in assessing the context of recently made decisions (Buckley et al., 2009). The ACC is positioned to mediate signal transfer towards and away from the hippocampus as demonstrated physiologically by a process that is not well understood (Paz et al., 2007). Our results speak to the circuit mechanisms for this process, namely, possible facilitated access of the ACC pathway to the hippocampus via large synapses, as well as association with CR inhibitory neurons which are thought to disinhibit the local network in the upper cortical layers (del Rio and DeFelipe, 1997). Thus, pathways from ACC, which convey attentional signals and the context of events, can overcome the robust inhibition in the rhinal region to enable information that must be remembered to gain access to the hippocampus (Biella et al., 2002; de Curtis and Paré, 2004; Pelletier et al., 2004) or be sent from the hippocampus to other cortices.

Prefrontal pathways gate hippocampal output and may determine which memories endure

Here we showed that both ACC and pOFC pathways preferentially target PV-positive dendrites in the deep layers of rhinal cortices. The deep layers of entorhinal cortex give rise to the pathway through which emergent hippocampal output reaches the rest of the cortex. Projections from multimodal area 36 to unimodal sensory cortices also originate in the deep layers, according to the rules of the structural model for cortico-cortical connections (Barbas and Rempel-Clower, 1997), and consistent with empirical findings (Lavenex and Amaral, 2000). The entorhinal deep layers also serve as a potential point of reentrance into the hippocampal loop via an ascending excitatory pathway which targets nearly equal proportions of excitatory pyramidal and inhibitory neurons in the upper layers (Kloosterman et al., 2003a,b; van Haeften et al., 2003; Buckmaster et al., 2004).

In both animals and humans, hippocampal output is served by sharp wave bursts of CA3 neurons which elicit high-frequency (200 Hz) ripple oscillations synchronizing CA1 and the deep layers of the entorhinal cortex (Chrobak and Buzsaki, 1994, 1996). Sharp wave-ripple complexes are correlated with memory performance (Axmacher et al., 2008). Increased activity in the perirhinal and prefrontal cortices is associated with sharp wave-ripples, suggesting a mechanism by which hippocampal output reaches the rest of the cortex (Siapas and Wilson, 1998; Collins et al., 1999; reviewed in Chrobak et al., 2000). In the deep layers of the rhinal cortex, PV inhibitory neurons which innervate perisomatic sites of excitatory neurons may play a role in generating ripples in a manner similar to that proposed for the hippocampus proper (Ylinen et al., 1995). While hippocampal output can elicit deep to superficial communication in the rhinal cortices, little activity is observed in the upper layers following sharp-wave ripple events, likely due to the prominent feedforward inhibition evoked by the pathway (Chrobak and Buzsaki, 1994; Kloosterman et al., 2003a).

Our results suggest that, via their interaction with PV inhibitory targets in the deep layers, the prefrontal

pathways may be positioned to mediate when the ascending pathway in the entorhinal cortex is engaged and thereby determine the fate of hippocampal output. Attentional signals from the prefrontal cortex can drive activity in the deep layers of the rhinal cortex to transfer hippocampal output to other cortical areas presumably for memory storage. Alternatively, by driving PV inhibitory neurons in the deep layers, prefrontal attentional and emotional signals may inhibit propagation of hippocampal output and instead direct the signal to the upper layers via the ascending pathway while simultaneously disinhibiting the local circuit to allow signals back into the hippocampal loop. Several studies have demonstrated that propagation of signals within the rhinal cortices and onwards to the hippocampus is dependent on the synergistic effects of perirhinal cortex and the amygdala, mediated by activity in the deep layers of entorhinal cortex (Kajiwara et al., 2003; Koganezawa et al., 2008). Further, activity in the medial prefrontal cortex is correlated with increased firing in the rhinal cortices when learning a task, while the cortico-cortical transfer of information from the entorhinal to the perirhinal cortices is enhanced during the late stages of learning (Paz et al., 2007).

Prefrontal pathways to medial temporal areas in disease

Rhinal PV neurons are vulnerable in Alzheimer's disease (Solodkin et al., 1996), especially in the upper layers, which show marked pathology in the earliest stages of the disease, as do pyramidal neurons in layers 5 and 3 of pOFC and to some extent neurons in the ACC (Hyman et al., 1984; Arnold et al., 1991; Van Hoesen et al., 2000). This pattern suggests compromise of pathways that enter as well as exit the hippocampus in Alzheimer's disease, suggesting decline in multiple aspects of memory formation and long-term storage.

Disruption in the convergence of information pertaining to the external and internal environments and value of stimuli from pOFC, coupled with attentional modulation of context by ACC, may also help explain the symptoms in posttraumatic stress disorder (PTSD), which represents an amalgam of contextual, emotional, and mnemonic dysfunction. Imaging studies indicate that hyperarousal, flashbacks, dissociations, amnesias, and hypermnesias manifest due to disruptions in the ACC-rhinal circuit leading to an inability to accurately integrate context with emotionally salient memories (Van Der Kolk et al., 1997; Rauch et al., 2006; Tsoory et al., 2008). These relationships have been noted with electrical stimulation of the temporal cortices that elicits an "alteration in the usual mechanism of comparison of immediate sensory perception with memory records" (Penfield and Rasmussen, 1957). The classical findings demonstrate that such manipulations can induce dissociative responses that are similar to those observed in patients suffering from PTSD (reviewed in Lanius et al., 2006). Recent imaging findings show a localized region in the rhinal cortex (perhaps area 35) which is involved in memory for item-context associations (Watson et al., 2012). Dysfunction in this circuit could help explain the contextual disconnection and symptoms of reexperiencing emotional episodes in anxiety disorders. Our findings suggest that synergism between pathways from pOFC and ACC within medial temporal cortices may be critical for interpreting emotional signals within the appropriate context for normal function.

CONCLUSION

The present findings suggest that the attentional context provided by the ACC pathway robustly affects mnemonic processes through large and efficient synapses that excite and disinhibit the rhinal network in the upper layers, the cortical gateway to the hippocampus. The pOFC pathway may convey an attentional signal to help focus on motivationally relevant sensory stimuli in area 36, which in turn mediates information flow to areas 35 and 28 and ultimately to the hippocampus. Together, the prefrontal pathways are positioned to overcome the rhinal wall of inhibition, allowing information to enter the hippocampus, as well as gate hippocampal output to the rest of cortex. Understanding how the ACC and pOFC signals impinge upon the medial temporal cortices and how attentional context is integrated with emotional and mnemonic information is critical for understanding memory function and disruption in psychiatric and neurologic disorders, such as PTSD and Alzheimer's disease.

CONFLICT OF INTEREST

None.

ROLE OF AUTHORS

All authors had access to the data in the study and take responsibility for the integrity and the accuracy of the data analysis. Study concept and design: JGB, BZ, HB. Acquisition of data: JGB, BZ, MF. Analysis and

interpretation of data: JGB, BZ, HB. Drafting of the article: JGB, BZ, MF, HB. Critical revision for the important intellectual content: JGB, BZ, MF, HB.

LITERATURE CITED

Ainsworth M, Lee S, Cunningham MO, Roopun AK, Traub RD, Kopell NJ, Whittington MA. 2011. Dual gamma rhythm generators control interlaminar synchrony in auditory cortex. J Neurosci 31:17040–17051.

Ainsworth M, Lee S, Cunningham MO, Traub RD, Kopell NJ, Whittington MA. 2012. Rates and rhythms: a synergistic view of frequency and temporal coding in neuronal networks. Neuron 75:572–583.

Airaksinen MS, Eilers J, Garaschuk O, Thoenen H, Konnerth A, Meyer M. 1997. Ataxia and altered dendritic calcium signaling in mice carrying a targeted null mutation of the calbindin D28k gene. Proc Natl Acad Sci U S A 94:1488–1493.

Amaral DG, Insausti R, Cowan WM. 1987. The entorhinal cortex of the monkey: I. Cytoarchitectonic organization. J Comp Neurol 264:326–355.

Anderson P, Lomo T. 1966. Mode of activation of hippocampal pyramidal cells by excitatory synapses on dendrites. Exp Brain Res 2:247–260.

Apergis-Schoute J, Pinto A, Paré D. 2006. Ultrastructural organization of medial prefrontal inputs to the rhinal cortices. Eur J Neurosci 24:135–144.

Arnold SE, Hyman BT, Flory J, Damasio AR, Van Hoesen GW. 1991. The topographical and neuroanatomical distribution of neurofibrillary tangles and neuritic plaques in the cerebral cortex of patients with Alzheimer's disease. Cereb Cortex 1:103–116.

Axmacher N, Elger CE, Fell J. 2008. Ripples in the medial temporal lobe are relevant for human memory consolidation. Brain 131(Pt 7):1806–1817.

Bachevalier J, Nemanic S. 2008. Memory for spatial location and object-place associations are differently processed by the hippocampal formation, parahippocampal areas TH/TF and perirhinal cortex. Hippocampus 18:64–80.

Barbas H. 1993. Organization of cortical afferent input to orbitofrontal areas in the rhesus monkey. Neuroscience 56:841–864.

Barbas H. 1995. Anatomic basis of cognitive-emotional interactions in the primate prefrontal cortex. Neurosci Biobehav R 19:499–510.

Barbas H. 2000a. Complementary role of prefrontal cortical regions in cognition, memory and emotion in primates. Adv Neurol 84:87–110.

Barbas H. 2000b. Connections underlying the synthesis of cognition, memory, and emotion in primate prefrontal cortices. Brain Res Bull 52:319–330.

Barbas H. 2007. Flow of information for emotions through temporal and orbitofrontal pathways. J Anat 211:237–249.

Barbas H, Blatt GJ. 1995. Topographically specific hippocampal projections target functionally distinct prefrontal areas in the rhesus monkey. Hippocampus 5:511–533.

Barbas H, Pandya DN. 1989. Architecture and intrinsic connections of the prefrontal cortex in the rhesus monkey. J Comp Neurol 286:353–375.

Barbas H, Rempel-Clower N. 1997. Cortical structure predicts the pattern of corticocortical connections. Cereb Cortex 7:635–646.

Barbas H, Zikopoulos B. 2006. Sequential and parallel circuits for emotional processing in primate orbitofrontal cortex. In: David Z, Scott R, editors. The orbitofrontal cortex. Oxford, UK: Oxford University Press. p 57–91.

Barbas H, Ghashghaei H, Dombrowski SM, Rempel-Clower NL. 1999. Medial prefrontal cortices are unified by common connections with superior temporal cortices and distinguished by input from memory-related areas in the rhesus monkey. J Comp Neurol 410:343–367.

Barbas H, Saha S, Rempel-Clower N, Ghashghaei T. 2003. Serial pathways from primate prefrontal cortex to autonomic areas may influence emotional expression. BMC Neurosci 4:25.

Barbas H, Zikopoulos B, Timbie C. 2011. Sensory pathways and emotional context for action in primate prefrontal cortex. Biol Psychiatry 69:1133–1139.

Barbas H, Bunce JG, Medalla M. 2013. Prefrontal pathways that control attention. In: Stuss DT, Knight R, editors. Principles of frontal lobe functions, 2nd ed. Oxford, UK: Oxford University Press.

Biella G, Uva L, de Curtis M. 2002. Propagation of neuronal activity along the neocortical-perirhinal-entorhinal pathway in the guinea pig. J Neurosci 22:9972–9979.

Blatt GJ, Pandya DN, Rosene DL. 2003. Parcellation of cortical afferents to three distinct sectors in the parahippocampal gyrus of the rhesus monkey: an anatomical and neurophysiological study. J Comp Neurol 466:161–179.

Borgers C, Epstein S, Kopell NJ. 2008. Gamma oscillations mediate stimulus competition and attentional selection in a cortical network model. Proc Natl Acad Sci U S A 105:18023–18028.

Botvinick MM, Cohen JD, Carter CS. 2004. Conflict monitoring and anterior cingulate cortex: an update. Trends Cogn Sci 8:539–546.

Buckley MJ, Mansouri FA, Hoda H, Mahboubi M, Browning PGF, Kwok SC, Phillips A, Tanaka K. 2009. Dissociable components of rule-guided behavior depend on distinct medial and prefrontal regions. Science 325:52–58.

Buckmaster PS, Alonso A, Canfield DR, Amaral DG. 2004. Dendritic morphology, local circuitry, and intrinsic electrophysiology of principal neurons in the entorhinal cortex of macaque monkeys. J Comp Neurol 470:317–329.

Buffalo EA, Bellgowan PS, Martin A. 2006. Distinct roles for medial temporal lobe structures in memory for objects and their locations. Learn Mem 13:638–643.

Buffalo EA, Fries P, Landman R, Buschman TJ, Desimone R. 2011. Laminar differences in gamma and alpha coherence in the ventral stream. Proc Natl Acad Sci U S A 108:11262–11267.

Bunce JG, Barbas H. 2011. Prefrontal pathways target excitatory and inhibitory systems in memory-related medial temporal cortices. NeuroImage 55:1461–1474.

Burwell RD, Amaral DG. 1998. Perirhinal and postrhinal cortices of the rat: interconnectivity and connections with the entorhinal cortex. J Comp Neurol 391:293–321.

Canolty RT, Edwards E, Dalal SS, Soltani M, Nagarajan SS, Kirsch HE, Berger MS, Barbaro NM, Knight RT. 2006. High gamma power is phase-locked to theta oscillations in human neocortex. Science 313:1626–1628.

Carmichael ST, Price JL. 1994. Architectonic subdivision of the orbital and medial prefrontal cortex in the macaque monkey. J Comp Neurol 346:366–402.

Carmichael ST, Price JL. 1995. Limbic connections of the orbital and medial prefrontal cortex in macaque monkeys. J Comp Neurol 363:615–641.

Carr DB, Sesack SR. 1998. Callosal terminals in the rat prefrontal cortex: synaptic targets and association with GABA-immunoreactive structures. Synapse 29:193–205.

Cavada C, Company T, Tejedor J, Cruz-Rizzolo RJ, Reinoso-Suarez F. 2000. The anatomical connections of the macaque monkey orbitofrontal cortex. A review. Cereb Cortex 10:220–242.

Celio MR, Heizmann CW. 1981. Calcium-binding protein parvalbumin as a neuronal marker. Nature 293:300–302.

Celio MR, Baier W, Scharer L, de Viragh PA, Gerday C. 1988. Monoclonal antibodies directed against the calcium binding protein parvalbumin. Cell Calcium 9:81–86.

Celio MR, Baier W, Scharer L, Gregersen HJ, de Viragh PA, Norman AW. 1990. Monoclonal antibodies directed against the calcium binding protein calbindin D-28k. Cell Calcium 11:599–602.

Chrobak JJ, Buzsaki G. 1994. Selective activation of deep layer (V-VI) retrohippocampal cortical neurons during hippocampal sharp waves in the behaving rat. J Neurosci 14:6160–6170.

Chrobak JJ, Buzsaki G. 1996. High-frequency oscillations in the output networks of the hippocampal-entorhinal axis of the freely behaving rat. J Neurosci 16:3056–3066.

Chrobak JJ, Lorincz A, Buzsaki G. 2000. Physiological patterns in the hippocampo-entorhinal cortex system. Hippocampus 10:457–465.

Clark AM, Bouret S, Young AM, Richmond BJ. 2012. Intersection of reward and memory in monkey rhinal cortex. J Neurosci 32:6869–6877.

Clark AM, Bouret S, Young AM, Murray EA, Richmond BJ. 2013. Interaction between orbital prefrontal and rhinal cortex is required for normal estimates of expected value. J Neurosci 33:1833–1845.

Collins DR, Lang EJ, Paré D. 1999. Spontaneous activity of the perirhinal cortex in behaving cats. Neuroscience 89:1025–1039.

Davachi L, Mitchell JP, Wagner AD. 2003. Multiple routes to memory: distinct medial temporal lobe processes build item and source memories. Proc Natl Acad Sci U S A 100:2157–2162.

de Curtis M, Paré D. 2004. The rhinal cortices: a wall of inhibition between the neocortex and the hippocampus. Prog Neurobiol 74:101–110.

DeFelipe J. 1997. Types of neurons, synaptic connections and chemical characteristics of cells immunoreactive for calbindin-D28K, parvalbumin and calretinin in the neocortex. J Chem Neuroanat 14:1–19.

DeFelipe J, Hendry SH, Jones EG. 1989a. Synapses of double bouquet cells in monkey cerebral cortex visualized by calbindin immunoreactivity. Brain Res 503:49–54.

DeFelipe J, Hendry SH, Jones EG. 1989b. Visualization of chandelier cell axons by parvalbumin immunoreactivity in monkey cerebral cortex. Proc Natl Acad Sci U S A 86:2093–2097.

del Rio MR, DeFelipe J. 1997. Synaptic connections of calretinin-immunoreactive neurons in the human neocortex. J Neurosci 17:5143–5154.

Disney AA, Aoki C. 2008. Muscarinic acetylcholine receptors in macaque V1 are most frequently expressed by parvalbumin-immunoreactive neurons. J Comp Neurol 507:1748–1762.

Dombrowski SM, Hilgetag CC, Barbas H. 2001. Quantitative architecture distinguishes prefrontal cortical systems in the rhesus monkey. Cereb Cortex 11:975–988.

Fell J, Klaver P, Lehnertz K, Grunwald T, Schaller C, Elger CE, Fernandez G. 2001. Human memory formation is accompanied by rhinal-hippocampal coupling and decoupling. Nat Neurosci 4:1259–1264.

Fell J, Ludowig E, Staresina BP, Wagner T, Kranz T, Elger CE, Axmacher N. 2011. Medial temporal theta/alpha power enhancement precedes successful memory encoding: evidence based on intracranial EEG. J Neurosci 31:5392–5397.

Ferdinand NK, Mecklinger A, Kray J, Gehring WJ. 2012. The processing of unexpected positive response outcomes in the mediofrontal cortex. J Neurosci 32:12087–12092.

Fiala JC. 2005. Reconstruct: a free editor for serial section microscopy. J Microsc Oxford 218(Pt 1):52–61.

Gabbott PL, Bacon SJ. 1996. Local circuit neurons in the medial prefrontal cortex (areas 24a,b,c, 25 and 32) in the monkey: I. Cell morphology and morphometrics. J Comp Neurol 364:567–608.

Germuska M, Saha S, Fiala JC, Barbas H. 2006. Synaptic distinction of laminar specific prefrontal-temporal pathways in primates. Cereb Cortex 16:865–875.

Gonchar Y, Burkhalter A. 2003. Distinct GABAergic targets of feedforward and feedback connections between lower and higher areas of rat visual cortex. J Neurosci 23:10904–10912.

Gundersen HJG, Bagger P, Bendtsen TF, Evans SM, Korbo L, Marcussen N, Moller A, Nielsen K, Nyengaard JR, Pakkenberg B, Sorensen FB, Vesterby A, West MJ. 1988. The new stereological tools: disector, fractionator, nucleator and point sample intercepts and their use in pathological research and diagnosis. Acta Patholog Microb 96:857–881.

Hayden BY, Platt ML. 2006. Fool me once, shame on me—fool me twice, blame the ACC. Nat Neurosci 9:857–859.

Hendry SHC, Jones EG, Emson PC, Lawson DEM, Heizmann CW, Streit P. 1989. Two classes of cortical GABA neurons defined by differential calcium binding protein immunoreactivities. Exp Br Res 76:467–472.

Hirano AA, Brandstatter JH, Morgans CW, Brecha NC. 2011. SNAP25 expression in mammalian retinal horizontal cells. J Comp Neurol 519:972–988.

Hoistad M, Barbas H. 2008. Sequence of information processing for emotions through pathways linking temporal and insular cortices with the amygdala. Neuroimage 40:1016–1033.

Howard CV, Reed MG. 1998. Unbiased stereology, three-dimensional measurement in microscopy. Oxford, UK: BIOS Scientific.

Hyman BT, Van Hoesen GW, Damasio AR, Barnes CL. 1984. Alzheimer's disease: cell-specific pathology isolates the hippocampal formation. Science 225:1168–1170.

Hyman JM, Ma L, Balaguer-Ballester E, Durstewitz D, Seamans JK. 2012. Contextual encoding by ensembles of medial prefrontal cortex neurons. Proc Natl Acad Sci U S A 109:5086–5091.

Imura K, Rockland KS. 2006. Long-range interneurons within the medial pulvinar nucleus of macaque monkeys. J Comp Neurol 498:649–666.

Insausti R, Amaral DG. 2008. Entorhinal cortex of the monkey: IV. Topographical and laminar organization of cortical afferents. J Comp Neurol 509:608–641.

Insausti R, Amaral DG, Cowan WM. 1987. The entorhinal cortex of the monkey: II. Cortical afferents. J Comp Neurol 264:356–395.

Isaacson JS, Scanziani M. 2011. How inhibition shapes cortical activity. Neuron 72:231–243.

Jutras MJ, Buffalo EA. 2010. Synchronous neural activity and memory formation. Curr Opin Neurobiol 20:150–155.

Jutras MJ, Fries P, Buffalo EA. 2009. Gamma-band synchronization in the macaque hippocampus and memory formation. J Neurosci 29:12521–12531.

Kajiwara R, Takashima I, Mimura Y, Witter MP, Iijima T. 2003. Amygdala input promotes spread of excitatory neural activity from perirhinal cortex to the entorhinal-hippocampal circuit. J Neurophysiol 89:2176–2184.

Kaping D, Vinck M, Hutchison RM, Everling S, Womelsdorf T. 2011. Specific contributions of ventromedial, anterior cingulate, and lateral prefrontal cortex for attentional selection and stimulus valuation. PLoS Biol 9:e1001224.

Kennerley SW, Walton ME, Behrens TE, Buckley MJ, Rushworth MF. 2006. Optimal decision making and the anterior cingulate cortex. Nat Neurosci 9:940–947.

Kloosterman F, van Haeften T, Witter MP, Lopes da Silva FH. 2003a. Electrophysiological characterization of interlaminar entorhinal connections: an essential link for re-entrance in the hippocampal-entorhinal system. Eur J Neurosci 18:3037–3052.

Kloosterman F, Witter MP, Van Haeften T. 2003b. Topographical and laminar organization of subicular projections to the parahippocampal region of the rat. J Comp Neurol 455:156–171.

Koganezawa N, Taguchi A, Tominaga T, Ohara S, Tsutsui K, Witter MP, Iijima T. 2008. Significance of the deep layers of entorhinal cortex for transfer of both perirhinal and amygdala inputs to the hippocampus. Neurosci Res 61: 172–181.

Kondo H, Saleem KS, Price JL. 2003. Differential connections of the temporal pole with the orbital and medial prefrontal networks in macaque monkeys. J Comp Neurol 465: 499–523.

Kondo H, Saleem KS, Price JL. 2005. Differential connections of the perirhinal and parahippocampal cortex with the orbital and medial prefrontal networks in macaque monkeys. J Comp Neurol 493:479–509.

Kosel KC, Van Hoesen GW, Rosene DL. 1982. Non-hippocampal cortical projections from the entorhinal cortex in the rat and rhesus monkey. Brain Res 244:201–213.

Lanius RA, Bluhm R, Lanius U, Pain C. 2006. A review of neuroimaging studies in PTSD: heterogeneity of response to symptom provocation. J Psychiat Res 40:709–729.

Lavenex P, Amaral DG. 2000. Hippocampal-neocortical interaction: a hierarchy of associativity. Hippocampus 10:420–430.

Lavenex P, Suzuki WA, Amaral DG. 2002. Perirhinal and parahippocampal cortices of the macaque monkey: projections to the neocortex. J Comp Neurol 447:394–420.

Lavenex P, Suzuki WA, Amaral DG. 2004. Perirhinal and parahippocampal cortices of the macaque monkey: intrinsic projections and interconnections. J Comp Neurol 472: 371–394.

Lavenex P, Lavenex PB, Bennett JL, Amaral DG. 2009. Postmortem changes in the neuroanatomical characteristics of the primate brain: hippocampal formation. J Comp Neurol 512:27–51.

MacDonald AW III, Cohen JD, Stenger VA, Carter CS. 2000. Dissociating the role of the dorsolateral prefrontal and anterior cingulate cortex in cognitive control. Science 288:1835–1838.

Majumdar S, Wassle H, Jusuf PR, Haverkamp S. 2008. Mirror-symmetrical populations of wide-field amacrine cells of the macaque monkey retina. J Comp Neurol 508:13–27.

Mangold JE, Hill DL. 2008. Postnatal reorganization of primary afferent terminal fields in the rat gustatory brainstem is determined by prenatal dietary history. J Comp Neurol 509:594–607.

Manns JR, Eichenbaum H. 2006. Evolution of declarative memory. Hippocampus 16:795–808.

Markram H, Toledo-Rodriguez M, Wang Y, Gupta A, Silberberg G, Wu C. 2004. Interneurons of the neocortical inhibitory system. Nat Rev Neurosci 5:793–807.

May OL, Hill DL. 2006. Gustatory terminal field organization and developmental plasticity in the nucleus of the solitary tract revealed through triple-fluorescence labeling. J Comp Neurol 497:658–669.

Medalla M, Barbas H. 2006. Diversity of laminar connections linking periarcuate and lateral intraparietal areas depends on cortical structure. Eur J Neurosci 23:161–179.

Medalla M, Barbas H. 2009. Synapses with inhibitory neurons differentiate anterior cingulate from dorsolateral prefrontal pathways associated with cognitive control. Neuron 61:609–620.

Medalla M, Barbas H. 2010. Anterior cingulate synapses in prefrontal areas 10 and 46 suggest differential influence in cognitive control. J Neurosci 30:16068–16081.

Medalla M, Barbas H. 2012. The anterior cingulate cortex may enhance inhibition of lateral prefrontal cortex via m2 cholinergic receptors at dual synaptic sites. J Neurosci 32:15611–15625.

Medalla M, Lera P, Feinberg M, Barbas H. 2007. Specificity in inhibitory systems associated with prefrontal pathways to temporal cortex in primates. Cereb Cortex 17(Suppl 1):i136–i150.

Melchitzky DS, Eggan SM, Lewis DA. 2005. Synaptic targets of calretinin-containing axon terminals in macaque monkey prefrontal cortex. Neuroscience 130:185–195.

Meskenaite V. 1997. Calretinin-immunoreactive local circuit neurons in area 17 of the cynomolgus monkey, *Macaca fascicularis*. J Comp Neurol 379:113–132.

Mikkonen M, Soininen H, Pitkanen A. 1997. Distribution of parvalbumin-, calretinin-, and calbindin-D28k-immunoreactive neurons and fibers in the human entorhinal cortex. J Comp Neurol 388:64–88.

Miller LM, Schreiner CE. 2000. Stimulus-based state control in the thalamocortical system. J Neurosci 20:7011–7016.

Mishkin M, Murray EA. 1994. Stimulus recognition. Curr Opin Neurobiol 4:200–206.

Mohedano-Moriano A, Pro-Sistiaga P, Arroyo-Jimenez MM, Artacho-Perula E, Insausti AM, Marcos P, Cebada-Sanchez S, Martinez-Ruiz J, Munoz M, Blaizot X, Martinez-Marcos A, Amaral DG, Insausti R. 2007. Topographical and laminar distribution of cortical input to the monkey entorhinal cortex. J Anat 211:250–260.

Mohedano-Moriano A, Martinez-Marcos A, Pro-Sistiaga P, Blaizot X, Arroyo-Jimenez MM, Marcos P, Artacho-Perula E, Insausti R. 2008. Convergence of unimodal and polymodal sensory input to the entorhinal cortex in the fascicularis monkey. Neuroscience 151:255–271.

Moore CT, Wilson CG, Mayer CA, Acquah SS, Massari VJ, Haxhiu MA. 2004. A GABAergic inhibitory microcircuit controlling cholinergic outflow to the airways. J Appl Physiol 96:260–270.

Morecraft RJ, Geula C, Mesulam MM. 1992. Cytoarchitecture and neural afferents of orbitofrontal cortex in the brain of the monkey. J Comp Neurol 323:341–358.

Munoz M, Insausti R. 2005. Cortical efferents of the entorhinal cortex and the adjacent parahippocampal region in the monkey (*Macaca fascicularis*). Eur J Neurosci 22: 1368–1388.

Murray EA, Wise SP. 2012. Why is there a special issue on perirhinal cortex in a journal called hippocampus? The perirhinal cortex in historical perspective. Hippocampus 22:1941–1951.

Murthy VN, Sejnowski TJ, Stevens CF. 1997. Heterogeneous release properties of visualized individual hippocampal synapses. Neuron 18:599–612.

Ohyama K, Sugase-Miyamoto Y, Matsumoto N, Shidara M, Sato C. 2012. Stimulus-related activity during conditional associations in monkey perirhinal cortex neurons depends on upcoming reward outcome. J Neurosci 32: 17407–17419.

Pandya DN, Van Hoesen GW, Mesulam MM. 1981. Efferent connections of the cingulate gyrus in the rhesus monkey. Exp Brain Res 42:319–330.

Paz R, Bauer EP, Paré D. 2007. Learning-related facilitation of rhinal interactions by medial prefrontal inputs. J Neurosci 27:6542–6551.

Pelletier JG, Apergis J, Paré D. 2004. Low-probability transmission of neocortical and entorhinal impulses through the perirhinal cortex. J Neurophysiol 91:2079–2089.

Penfield W, Rasmussen T. 1957. The cerebral cortex of man: a clinical study of localization of function, 4th ed. New York: Macmillan. p 157–181.

Peters A, Palay SL. 1996. The morphology of synapses. J Neurocytol 25:687–700.

Peters A, Palay SL, Webster HD. 1991. The fine structure of the nervous system. Neurons and their supporting cells. New York: Oxford University Press.

Pinto A, Jankowski M, Sesack SR. 2003. Projections from the paraventricular nucleus of the thalamus to the rat prefrontal cortex and nucleus accumbens shell: ultrastructural characteristics and spatial relationships with dopamine afferents. J Comp Neurol 459:142–155.

Pitkanen A, Amaral DG. 1993. Distribution of parvalbumin-immunoreactive cells and fibers in the monkey temporal lobe: The hippocampal formation. J Comp Neurol 331:37–74.

Rauch SL, Dougherty DD, Malone D, Rezai A, Friehs G, Fischman AJ, Alpert NM, Haber SN, Stypulkowski PH, Rise MT, Rasmussen SA, Greenberg BD. 2006. A functional neuroimaging investigation of deep brain stimulation in patients with obsessive-compulsive disorder. J Neurosurg 104:558–565.

Rempel-Clower NL, Barbas H. 2000. The laminar pattern of connections between prefrontal and anterior temporal cortices in the rhesus monkey is related to cortical structure and function. Cereb Cortex 10:851–865.

Rockland KS, Van Hoesen GW. 1999. Some temporal and parietal cortical connections converge in CA1 of the primate hippocampus. Cereb Cortex 9:232–237.

Rosene DL, Van Hoesen GW. 1977. Hippocampal efferents reach widespread areas of cerebral cortex and amygdala in the rhesus monkey. Science 198:315–317.

Rosenmund C, Stevens CF. 1996. Definition of the readily releasable pool of vesicles at hippocampal synapses. Neuron 16:1197–1207.

Rostkowski AB, Teppen TL, Peterson DA, Urban JH. 2009. Cell-specific expression of neuropeptide Y Y1 receptor immunoreactivity in the rat basolateral amygdala. J Comp Neurol 517:166–176.

Rudebeck PH, Behrens TE, Kennerley SW, Baxter MG, Buckley MJ, Walton ME, Rushworth MF. 2008. Frontal cortex subregions play distinct roles in choices between actions and stimuli. J Neurosci 28:13775–13785.

Rushworth MF, Buckley MJ, Behrens TE, Walton ME, Bannerman DM. 2007. Functional organization of the medial frontal cortex. Curr Opin Neurobiol 17:220–227.

Saleem KS, Logothetis NK. 2007. A combined MRI and histology atlas of the rhesus monkey brain in stereotaxic coordinates. London: Academic Press.

Saleem KS, Kondo H, Price JL. 2008. Complementary circuits connecting the orbital and medial prefrontal networks with the temporal, insular, and opercular cortex in the macaque monkey. J Comp Neurol 506:659–693.

Sallet J, Quilodran R, Rothe M, Vezoli J, Joseph JP, Procyk E. 2007. Expectations, gains, and losses in the anterior cingulate cortex. Cogn Affect Behav Ne 7:327–336.

Saunders RC, Vann SD, Aggleton JP. 2012. Projections from Gudden's tegmental nuclei to the mammillary body region in the cynomolgus monkey (*Macaca fascicularis*). J Comp Neurol 520:1128–1145.

Schiffmann SN, Cheron G, Lohof A, d'Alcantara P, Meyer M, Parmentier M, Schurmans S. 1999. Impaired motor coordination and Purkinje cell excitability in mice lacking calretinin. Proc Natl Acad Sci U S A 96:5257–5262.

Schindelin J, Arganda-Carreras I, Frise E, Kaynig V, Longair M, Pietzsch T, Preibisch S, Rueden C, Saalfeld S, Schmid B, Tinevez JY, White DJ, Hartenstein V, Eliceiri K, Tomancak P, Cardona A. 2012. Fiji: an open-source platform for biological-image analysis. Nat Methods 9:676–682.

Schwaller B, Bruckner G, Celio MR, Hartig W. 1999. A polyclonal goat antiserum against the calcium-binding protein calretinin is a versatile tool for various immunochemical techniques. J Neurosci Meth 92:137–144.

Sederberg PB, Kahana MJ, Howard MW, Donner EJ, Madsen JR. 2003. Theta and gamma oscillations during encoding predict subsequent recall. J Neurosci 23:10809–10814.

Seltzer B, Pandya DN. 1978. Afferent cortical connections and architectonics of the superior temporal sulcus and surrounding cortex in the rhesus monkey. Brain Res 149:1–24.

Siapas AG, Wilson MA. 1998. Coordinated interactions between hippocampal ripples and cortical spindles during slow-wave sleep. Neuron 21:1123–1128.

Solodkin A, Veldhuizen SD, Van Hoesen GW. 1996. Contingent vulnerability of entorhinal parvalbumin-containing neurons in Alzheimer's disease. J Neurosci 16:3311–3321.

Somogyi P, Tamas G, Lujan R, Buhl EH. 1998. Salient features of synaptic organisation in the cerebral cortex. Brain Res Brain Res Rev 26:113–135.

Squire LR, Zola-Morgan S. 1991. The medial temporal lobe memory system. Science 253:1380–1386.

Squire LR, Zola SM. 1996. Structure and function of declarative and nondeclarative memory systems. Proc Natl Acad Sci U S A 93:13515–13522.

Stevens CF. 2003. Neurotransmitter release at central synapses. Neuron 40:381–388.

Steward O, Scoville SA. 1976. Cells of origin of entorhinal cortical afferents to the hippocampus and fascia dentata of the rat. J Comp Neurol 169:347–370.

Stewart WW. 1981. Lucifer dyes—highly fluorescent dyes for biological tracing. Nature 292:17–21.

Suzuki WA. 2006. Encoding new episodes and making them stick. Neuron 50:19–21.

Suzuki WA. 2007. Making new memories: the role of the hippocampus in new associative learning. Ann N Y Acad Sci 1097:1–11.

Suzuki WA. 2010. Untangling memory from perception in the medial temporal lobe. Trends Cogn Sci 14:195–200.

Suzuki WA, Amaral DG. 1994a. Perirhinal and parahippocampal cortices of the macaque monkey: cortical afferents. J Comp Neurol 350:497–533.

Suzuki WA, Amaral DG. 1994b. Topographic organization of the reciprocal connections between the monkey entorhinal cortex and the perirhinal and parahippocampal cortices. J Neurosci 14:1856–1877.

Swanson LW, Kohler C. 1986. Anatomical evidence for direct projections from the entorhinal area to the entire cortical mantle in the rat. J Neurosci 6:3010–3023.

Tomioka R, Rockland KS. 2007. Long-distance corticocortical GABAergic neurons in the adult monkey white and gray matter. J Comp Neurol 505:526–538.

Tong G, Jahr CE. 1994. Multivesicular release from excitatory synapses of cultured hippocampal neurons. Neuron 12:51–59.

Tsoory MM, Vouimba RM, Akirav I, Kavushansky A, Avital A, Richter-Levin G. 2008. Amygdala modulation of memory-related processes in the hippocampus: potential relevance to PTSD. Prog Brain Res 167:35–51.

Van Der Kolk BA, Burbridge JA, Suzuki J. 1997. The psychobiology of traumatic memory. Clinical implications of neuroimaging studies. Ann NY Acad Sci 821:99–113.

van Haeften T, Baks-te-Bulte L, Goede PH, Wouterlood FG, Witter MP. 2003. Morphological and numerical analysis of synaptic interactions between neurons in deep and

superficial layers of the entorhinal cortex of the rat. Hippocampus 13:943–952.

Van Hoesen GW, Pandya DN. 1975. Some connections of the entorhinal (area 28) and perirhinal (area 35) cortices of the rhesus monkey. I. Temporal lobe afferents. Brain Res 95:1–24.

Van Hoesen GW, Pandya DN, Butters N. 1972. Cortical afferents to the entorhinal cortex of the rhesus monkey. Science 175:1471–1473.

Van Hoesen GW, Pandya DN, Butters N. 1975. Some connections of the entorhinal (area 28) and perirhinal (area 35) cortices of the rhesus monkey. II. Frontal lobe afferents. Brain Res 95:25–38.

Van Hoesen GW, Parvizi J, Chu CC. 2000. Orbitofrontal cortex pathology in Alzheimer's disease. Cereb Cortex 10:243–251.

Veenman CL, Reiner A, Honig MG. 1992. Biotinylated dextran amine as an anterograde tracer for single- and double-labeling studies. J Neurosci Meth 41:239–254.

Walker AE. 1940. A cytoarchitectural study of the prefrontal area of the macaque monkey. J Comp Neurol 73:59–86.

Walmsley B, Alvarez FJ, Fyffe RE. 1998. Diversity of structure and function at mammalian central synapses. Trends Neurosci 21:81–88.

Wang XJ, Tegner J, Constantinidis C, Goldman-Rakic PS. 2004. Division of labor among distinct subtypes of inhibitory neurons in a cortical microcircuit of working memory. Proc Natl Acad Sci U S A 101:1368–1373.

Watson HC, Wilding EL, Graham KS. 2012. A role for perirhinal cortex in memory for novel object-context associations. J Neurosci 32:4473–4481.

Weible AP. 2013. Remembering to attend: The anterior cingulate cortex and remote memory. Behav Brain Res 15:63–75.

Wellman BJ, Rockland KS. 1997. Divergent cortical connections to entorhinal cortex from area TF in the macaque. J Comp Neurol 389:361–376.

Wirth S, Yanike M, Frank LM, Smith AC, Brown EN, Suzuki WA. 2003. Single neurons in the monkey hippocampus and learning of new associations. Science 300:1578–1581.

Witter MP, Van Hoesen GW, Amaral DG. 1989. Topographical organization of the entorhinal projection to the dentate gyrus of the monkey. J Neurosci 9:216–228.

Womelsdorf T, Fries P. 2007. Neuronal coherence during selective attentional processing and sensory-motor integration. J Physiol Paris 100:182–193.

Xu X, Roby KD, Callaway EM. 2010. Immunochemical characterization of inhibitory mouse cortical neurons: three chemically distinct classes of inhibitory cells. J Comp Neurol 518:389–404.

Ylinen A, Bragin A, Nadasdy Z, Jando G, Szabo I, Sik A, Buzsaki G. 1995. Sharp wave-associated high-frequency oscillation (200 Hz) in the intact hippocampus: network and intracellular mechanisms. J Neurosci 15(1 Pt 1):30–46.

Zaitsev AV, Gonzalez-Burgos G, Povysheva NV, Kroner S, Lewis DA, Krimer LS. 2005. Localization of calcium-binding proteins in physiologically and morphologically characterized interneurons of monkey dorsolateral prefrontal cortex. Cereb Cortex 15:1178–1186.

Zikopoulos B, Barbas H. 2006. Prefrontal projections to the thalamic reticular nucleus form a unique circuit for attentional mechanisms. J Neurosci 26:7348–7361.

Zikopoulos B, Barbas H. 2007. Parallel driving and modulatory pathways link the prefrontal cortex and thalamus PLoS One 2:e848.

Zikopoulos B, Barbas H. 2012. Pathways for emotions and attention converge on the thalamic reticular nucleus in primates. J Neurosci 32:5338–5350.

Zimmermann L, Schwaller B. 2002. Monoclonal antibodies recognizing epitopes of calretinins: dependence on Ca2+-binding status and differences in antigen accessibility in colon cancer cells. Cell Calcium 31:13–25.